Eidgenössische Technische Hochschule Zürich
Swiss Federal Institute of Technology Zurich

Master thesis

Generation of amplitude and phase controlled microwave pulses for qubit manipulation in Circuit QED

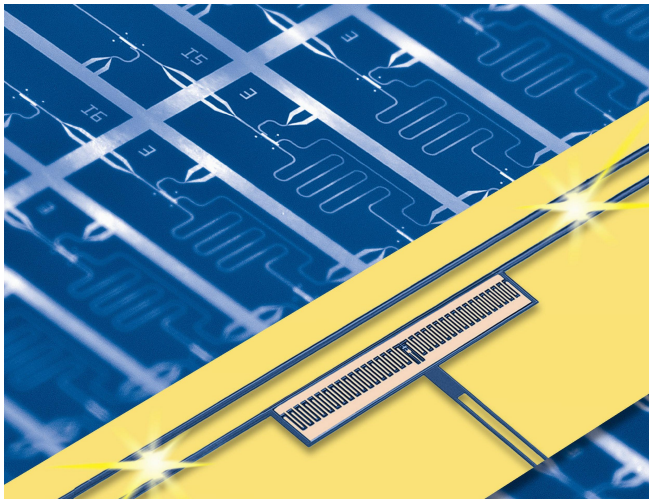

Presented by: Simon Schmidlin
Supervisor: Dr. Peter Leek
Handed-in to: Prof. Dr. Andreas Wallraff,
Laboratory for Solid State Physics, ETH Zürich

Zürich, March 4, 2009

Contents

1 Introduction

Since 1960, Gordon Moore's law, which states that the computer power will double every two years for constant cost, held true. But one will expect that this will end some time, since the fabrication of computer hardware will have fundamental difficulties due to its tiny size. Which means that quantum effects will be observable and interfere in the functionality of the electronic devices. In 1982, Richard Feynman had the idea to make use of the quantum mechanics in a so-called *quantum computer*, such that it might perform more powerful calculations than a classical computer. It's not that easy to realize such a quantum computer, based on the fundamental units of information, the so called *quantum bits*, qubits.[17] Qubits do not only take the value 0 or 1 like the classical bits, it is in a linear superposition of those two states. If one writes the ground state of a quantum system as $|0\rangle$ and the excited state as $|1\rangle$, the qubit can be written as a combination of them and is represented by a vector contained in a sphere (Bloch sphere), see section 2.2.
The implementation of such a qubit requires a quantum mechanical two-level system that can be well controlled and measured. A physical state will always have some interaction with its environment. Due to this external influence, a pure superposition state $(|0\rangle \pm |1\rangle)/\sqrt{2}$ has a time-development into the state $|0\rangle$, which is equivalent to a collapse of the superposition state. This loss of the superposition property of a quantum state is called decoherence. It's one of the main problem in building quantum computers. A good isolation of the qubit from its environment is therefore necessary (beside the preparing and readout of the qubit-state), such that it has a long decoherence time, which allows to perform many operations before the superposition state is destroyed. An other important time scale is the so called relaxation time: If one leaves a system to its own, it tend to the state of lowest energy. David DiVincenzo, of IBM, listed the following requirements for a practical quantum computer:

- scalable physically to increase the number of qubits
- qubits can be initialized to arbitrary values
- quantum gate-operation time shorter than decoherence time
- universal set of quantum gates
- each qubit-state can be read-out easily

A quantum gate is a basic quantum circuit operating on a small number of qubits.[5]

1.1 Superconducting circuits

The theory of quantum mechanics was originally developed to account for the observed behaviour of electrons in atoms. More than 80 years later, it is being used to explain the behaviour of superconducting circuits that can be hundreds of nanometers in size and can contain trillions of electrons. The quantum nature of these circuits is observable because they can be engineered to be isolated from the electrical environment. Unlike atoms, these circuits can be designed and constructed to tailor their characteristic frequencies, as well as other parameters like the energy gap between the ground- and excited state. Superconducting qubits form the key component of these circuits, where its state can be manipulated by using electromagnetic pulses. One promising approach toward quantum computers which allows to isolate the qubits efficiently from the environment while still providing good measurement and control possibilities is called circuit quantum electrodynamics (cQED). A charge qubit is formed by a tiny superconducting island (Cooper-pair box) coupled by a Josephson junction to a superconducting reservoir. The Cooper pair box is strongly coupled to a microwave cavity, which is realised with a coplanar transmission line resonator. By applying microwave signals to the resonator, one can couple the photons in the cavity to the qubit, which allows to control or measure the qubit state. In contrast to other candidates like trapped ions or quantum dots where the qubits are built on single quantum objects (i.e. microscopic systems) one uses a macroscopic object in cQED. The quantum behavior of a macroscopic system is usually not observable, although each particle in a given system behaves quantum mechanically. This has to do with the Fermi-Dirac-Statistic of identical Fermions without mutual interaction, which predict that no two fermions can occupy the same energy-state. It's only possible to observe quantum mechanical behavior in a macroscopic system if the component particles populate the same state, i.e. if they obey the Bose-Einstein-Statistics. Two prominent examples of such systems are Bose-Einstein condensates and superconductors. In a conventional superconductor, the electronic fluid consists of bound pairs of electrons known as Cooper pairs. This pairing is caused by an attractive force

between electrons due to the exchange of phonons. The Cooper pairs are then condensed into one single state with a defined phase $\Theta(\vec{r},t)$ and a local density n_s of the superconducting entities

$$|\Psi\rangle = \sqrt{n_s(\vec{r},t)}\, e^{i\,\Theta(\vec{r},t)} \tag{1.1}$$

A Cooper-pair box (CPB) can be used to form a non-linear two-level system which is then strongly coupled to a single mode of an electromagnetic field. It's important to a have a system which is non-linear, otherwise one can't see any difference between the classical and the quantum mechanical behavior. This can be seen by considering the Ehrenfest-Theorem, which predict the classical relation of motion for the expectation value of any quantum mechanical observable if the potential is of quadratic form in position (i.e. harmonic oscillator). The analog of the position in a electrical harmonic oscillator is the magnetic flux Φ. By analysing an electrical LC oscillator and comparing it to an mechanical oscillator one got the following correspondences

	mechanical oscillator	electrical LC oscillator
momentum	$p_x(t)$	$q(t)$
position	$x(t)$	$\Phi(t)$
mass	m	C
frequency	$\sqrt{k/m}$	$1/\sqrt{L\,C}$
commutator	$[x,p_x]=i\hbar$	$[\Phi,q]=i\hbar$

Table 1.1: Correspondence table of a one-dimensional mechanical oscillator and an electrical LC oscillator circuit.[7]

It's therefore necessary to have a nonlinear system to even measure non-classical effects. In cQED this is realised with a Josephson junction which behave like an LC-circuit but the inductance L then build the nonlinearity.
We use superconducting materials to observe quantum effects on a single non-degenerate macroscopic ground state, another advantage of using such materials is the energy gap Δ in the excitation spectrum which makes it easier to stay in the ground state due to the elimination of low-energy excitations. The energy gap Δ is the minimum amount of energy that must be supplied to one Cooper pair in order to excite it. Our superconducting materials are Niobium (Nb) and Aluminum (Al)

	Niobium	Aluminum
critical Temperature T_c	9.2 K	1.2 K
$2\Delta/h$	725 GHz	100 GHz

Table 1.2: Characteristics of Niobium and Aluminum in the superconducting state.

The state of the qubit can be controlled by applying microwave pulses with a certain amplitude and phase. It's therefore desired to have a full amplitude- and phase

control of the pulses applied on the qubit. This can be done by using an IQ-mixer in the upconverting operative range. To reach this goal, a high degree of accuracy on the IQ-mixer calibration is necessary, which was the main task of the work. A demonstration of the full control was shown in a tomography experiment performed on one qubit. An other goal was to test a new setup to do sideband-operations, i.e. the $|g,0\rangle \rightarrow |e,1\rangle$ transition, with demonstrating phase sensitive measurements on this transition.

2 Theory

2.1 Quantum Bits

The classical bit is the unit of computer information and can only take the value 0 or 1, for example: the voltage level at the input of a transistor in a digital circuit. In contrast, a quantum bit (qubit) can also be in a superposition state

$$|\Phi\rangle = \alpha\,|0\rangle + \beta\,|1\rangle\,, \qquad |\alpha|^2 + |\beta|^2 = 1 \tag{2.1}$$

the second condition for the two complex probability amplitudes α and β makes sure that the sum over all probabilities of finding the qubit in any state is 1. When the state of a qubit is measured one will find the probability $|\alpha|^2$ to be in the state $|0\rangle$ and the a probability of $|\beta|^2$ to find it in state $|1\rangle$. A qubit can be represented as vectors in a 2-dimensional Hilbert space, where the Dirac notation is used as a set of orthonormal basis

$$|0\rangle \equiv \begin{pmatrix} 1 \\ 0 \end{pmatrix} \qquad |1\rangle \equiv \begin{pmatrix} 0 \\ 1 \end{pmatrix} \tag{2.2}$$

In a two level system, the state $|0\rangle$ is called *ground state*, where $|1\rangle$ is the *excited state*. There are a lot of different physical systems which can be used to realize qubits: the two different polarizations of a photon, the alignment of a nuclear spin in a uniform magnetic field, spin of a single electron and of course by a Josephson junction as shown later. The first postulate of quantum mechanics associated to any isolated physical system a complex vector space with an inner product (i.e. Hilbert space) which is known as the state space of the system, where the system is completely described by its unit state vector. The time evolution a such a state vector in a closed quantum system is described by the Schroedinger equation,

$$i\hbar \frac{d\,|\Phi\rangle}{dt} = \widehat{H}\,|\Phi\rangle \tag{2.3}$$

If the system is not closed anymore and interacts with its environment, the third postulate of quantum mechanics describes the effect of measurements on the system by operators acting on the state space [17].

2.2 Bloch sphere representation of qubit state space

The equation 2.1 can be rewritten using the additional condition

$$|\Phi\rangle = e^{i\gamma}\left(\cos\frac{\Theta}{2}|0\rangle + e^{i\phi}\sin\frac{\Theta}{2}|1\rangle\right) \tag{2.4}$$

where Θ, ϕ and γ are real numbers. The outer factor $e^{i\gamma}$ describes the global phase γ, which can be ignored, because it's impossible to measure it. This reduced equation then defines a point on the unit three-dimensional sphere, also called *Bloch sphere*. In this representation, Θ is called *polar angle* and ϕ defines the *azimuth angle*, see Figure 2.1 The ground state corresponds to a vector pointing on the north pole and

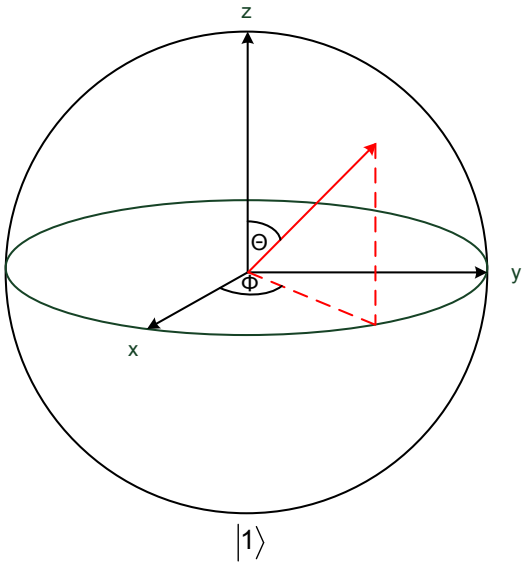

Figure 2.1: Bloch sphere representation of a qubit state.

the excited to the south pole. All the equal superposition state are located on the equator, i.e. $\frac{1}{\sqrt{2}}\left(|0\rangle + e^{i\phi}|1\rangle\right)$ A rotation around an arbitrary axis $\vec{n} = (n_x, n_y, n_z)$ with an angle α can be written as

$$R_{\vec{n}}(\alpha) \equiv exp\left(-i\alpha\vec{n}\cdot\vec{\sigma}/2\right), \qquad \vec{\sigma} = (I, X, Y, Z) \tag{2.5}$$

Where $\vec{\sigma}$ is the Pauli vector which consists of the 4 matrices given by

$$I \equiv \begin{pmatrix} 1 & 0 \\ 0 & 1 \end{pmatrix} \quad X \equiv \begin{pmatrix} 0 & 1 \\ 1 & 0 \end{pmatrix} \quad Y \equiv \begin{pmatrix} 0 & -i \\ i & 0 \end{pmatrix} \quad Z \equiv \begin{pmatrix} 1 & 0 \\ 0 & -1 \end{pmatrix} \tag{2.6}$$

This can now be used to prepare any specific qubit state. Let's take the ground state as the initial one and by applying a π-pulse the excited state can be reached

$$R_x\left(\Omega_x t = \pi\right) \quad : \qquad |0\rangle \longrightarrow |1\rangle \tag{2.7}$$

$$R_y\left(\Omega_y t = \pi\right) \quad : \qquad |0\rangle \longrightarrow -i\,|1\rangle \tag{2.8}$$

But it's also possible to prepare a superposition state with a $\pi/2$-pulse

$$R_x\left(\Omega_x t = \pi/2\right) \quad : \qquad |0\rangle \longrightarrow \frac{|0\rangle + |1\rangle}{\sqrt{2}} \tag{2.9}$$

$$R_y\left(\Omega_y t = \pi/2\right) \quad : \qquad |0\rangle \longrightarrow \frac{|0\rangle - i\,|1\rangle}{\sqrt{2}} \tag{2.10}$$

Notice that the angle α was replaced by the product of an angular velocity $\Omega_{x,y}$ and the pulse length t.

2.3 Realization of the superconducting qubits

To build a quantum electrical circuit it's necessary to have low dissipation, low thermal noise and the circuit has to be non-linear as already discussed in the introduction section. To reach this goal, one uses Josephson tunnel junctions which are made of superconducting and insulating materials and to avoid thermal noise, the experiment is operating at low temperature of about 20 mK.

2.3.1 Quantization of the electrical parallel LC harmonic oscillator

A parallel LC oscillator circuit consists of an inductor L where a magnetic flux ϕ is stored and a conductor C where the charge Q is accumulated on it, see Figure 2.2.

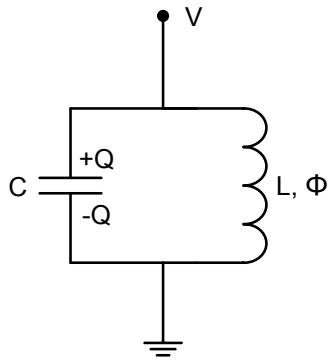

Figure 2.2: Circuit diagram of the parallel LC harmonic oscillator.

The voltage across the oscillator can therefore be written by

$$V = \frac{Q}{C} = -L\frac{\partial I}{\partial t} \tag{2.11}$$

where the time-varying current I is passing through it. The capacitor stores energy in the electric field between its plates, depending on the voltage across it, and the inductor stores energy in its magnetic field, depending on the current. By summarizing this two energies one gets

$$H = \frac{1}{2}CV^2 + \frac{1}{2}LI^2 = \frac{1}{2}\frac{Q^2}{C} + \frac{1}{2}\frac{\phi^2}{L} \tag{2.12}$$

since the inductance gives the linear relation between the magnetic flux and the current, i.e. $\phi = LI$. By considering the total energy as a Hamiltonian (i.e. the Legendre-transformation of the Lagrange-function) $H(Q, \phi, t)$, the equation of motion in a classical system can then be calculated by the derivative

$$\frac{\partial H}{\partial Q} = \frac{Q}{C} = -L\frac{\partial I}{\partial t} = -\dot{\phi} \tag{2.13}$$

$$\frac{\partial H}{\partial \phi} = \frac{\phi}{L} = I = \dot{Q} \tag{2.14}$$

Now, the two conjugated variables Q and ϕ can be replaced by its corresponding quantum mechanical operators

$$\phi \longrightarrow \hat{\phi} \tag{2.15}$$

$$Q \longrightarrow \hat{Q} = -i\hbar\frac{\partial}{\partial \phi} \tag{2.16}$$

So, the classical Hamilton-function can be replaced by the Hamilton operator $\hat{H}$

$$\hat{H} = \frac{\hat{Q}^2}{2C} + \frac{\hat{\phi}^2}{2L} = -\frac{\hbar^2}{2C}\frac{\partial^2}{\partial \phi^2} + \frac{\hat{\phi}^2}{2L} \tag{2.17}$$

Comparing this Hamilton operator with a particle in a harmonic potential which has

the following properties [20]

$$\begin{aligned}
\hat{H}_{HO} &= \frac{\hat{p}^2}{2m} + \frac{1}{2}m\omega^2\hat{x}^2 && (2.18)\\
&= \hbar\omega\left(\hat{a}^+\hat{a} + \frac{1}{2}\right) && (2.19)\\
[\hat{x}, \hat{p}] &= i\hbar && (2.20)\\
\hat{a} &\equiv \sqrt{\frac{m\omega}{2\hbar}}\left(\hat{x} + \frac{i\hat{p}}{m\omega}\right) && (2.21)\\
\hat{a^+} &\equiv \sqrt{\frac{m\omega}{2\hbar}}\left(\hat{x} - \frac{i\hat{p}}{m\omega}\right) && (2.22)
\end{aligned}$$

The raising $\hat{a}^+$ and lowering $\hat{a}$ operators act on the *Fock-state*, where the number of energy quanta $\hbar\omega$ can be in- or decreased by definition

$$\begin{aligned}
\hat{a}\,|n\rangle &= \sqrt{n}\,|n-1\rangle && (2.23)\\
\hat{a}^+\,|n\rangle &= \sqrt{n+1}\,|n+1\rangle && (2.24)
\end{aligned}$$

Due to this well known system of a linear quantum oscillator, one can compare it to the electrical analogy

$$\begin{aligned}
\hat{a} &= \frac{1}{\sqrt{2\hbar Z_c}}\left(Z_c\hat{Q} + i\hat{\phi}\right) && (2.25)\\
\hat{a^+} &= \frac{1}{\sqrt{2\hbar Z_c}}\left(Z_c\hat{Q} - i\hat{\phi}\right) && (2.26)\\
\hat{Q} &= \sqrt{\frac{\hbar}{2Z_c}}(a + a^+) && (2.27)\\
\hat{\phi} &= \sqrt{\frac{2Z_c}{\hbar}}(a - a^+) && (2.28)\\
Z_c &= \sqrt{\frac{L}{C}} && (2.29)\\
\left[\hat{\phi}, \hat{Q}\right] &= i\hbar && (2.30)\\
\omega &= \frac{1}{\sqrt{LC}} && (2.31)
\end{aligned}$$

Further relationships can be read out in tabel 1.1. Z_c is called *characteristic impedance* of the oscillator. The resonance frequency in our experiment is around $\omega \approx 2\pi\,6$ GHz and therefore the energy distance between two neighboring states correspond to a temperature of $\frac{\hbar\omega}{k_B} \approx 300\,\mathrm{mK}$, this is also the ground state energy. The calculated eigenstates of the Hamiltonian 2.17 are shown in Figure 2.3 for the first ten energy levels, depending on the magnetic flux. As mentioned in the Introduction is an equally separated energy spectrum improper to measure quantum mechanical effects since they will be averaged out. So on, it's necessary to have at least 2 states (ground- and

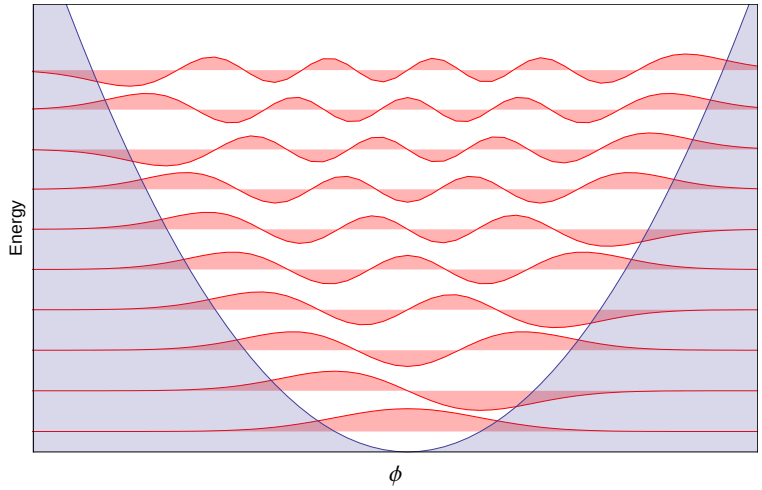

Figure 2.3: Wavefunction representations for the first ten eigenstates of the LC oscillator. The horizontal axis shows the magnetic flux ϕ and the vertical its corresponding energy.

excited) which have a different energy separation compared to higher energy states. To build an anharmonic spectrum one uses a Josephson junction, which yields an nonlinear inductance if added to the LC-oscillator.

2.3.2 Josephson junction

A Josephson junction is made of two superconducting materials separated by a tunneling barrier which is normal conducting. The Cooper pairs can now tunnel through this barrier if one applies a small current. But there is a critical current I_c above which the Cooper pairs will break open such that a resistance occurs due to the tunneling of single electrons and a voltage is therefore measurable. Each superconductor

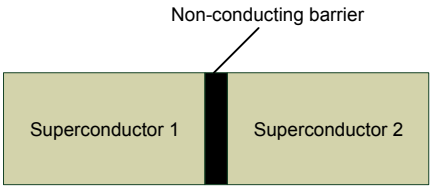

Figure 2.4: Schematic image of a Josephson junction. Theoretical prediction 1962 by Brian D. Josephson.

can be described by a single wave function which overlap another, but each wave function itself obey the Schroedinger equation

$$i\hbar\frac{\partial\Psi_1}{\partial t} = \hat{H}_1\Psi_1 + \kappa\Psi_2 \tag{2.32}$$

$$i\hbar\frac{\partial\Psi_2}{\partial t} = \hat{H}_2\Psi_2 + \kappa\Psi_1 \tag{2.33}$$

where κ expresses the coupling between the superconductors given by the tunnel barrier and $\hat{H}_1$ respectively $\hat{H}_2$ are the Hamilton operators acting on the corresponding wave function. [10] As mentioned before, this two wavefunctions Ψ_1, Ψ_2 overlap and gives rise to a phase difference across the junction $\delta(t)$ depending on time. The supercurrent through the tunnel barrier is then given by the 1.Josephson equation

$$I_s(t) = I_c \sin \delta(t) \tag{2.34}$$

Notice that even if there is no external voltage supply, a supercurrent is flowing, but equivalent cooper pairs are tunneling in each direction. The second Josephson equation describes the time behavior of $\delta(t)$ if an additional voltage $U(t)$ across the junction is applied

$$\frac{\partial \delta(t)}{\partial t} = \frac{2e}{\hbar} U(t) \tag{2.35}$$

$\frac{2e}{h}$ is called *Josephson constant* and is the inverse of a *magnetic flux quantum*. The three main effects predicted by Josephson follow from these equations [1]

1. **The DC Josephson effect**
   If there is no potential difference between the two superconductors, the phase doesn't varies in time given by the second Josephson equation

   $$U(t) = 0 \longrightarrow \delta(t) = \delta(t = 0) \longrightarrow I_s = I_c \sin \delta(t = 0) \tag{2.36}$$

   Now it's obvious that no net supercurrent is flowing, because of the alternating oscillation given by the sine function.

2. **The AC Josephson effect**
   With a constant voltage $U_{DC} \neq 0$ across the junction, the phase will vary linearly in time and the current is a sinusoidal AC at the Josephson frequency $2eU_{DC}/h$ with an amplitude given by the critical current I_c

   $$\delta(t) = \frac{2eU_{DC}}{\hbar} t + \delta(t = 0) \tag{2.37}$$

   $$f_J \equiv \frac{2eU_{DC}}{h} \tag{2.38}$$

   $$I_s = I_c \sin\left(2\pi f_J t + \delta(t = 0)\right) \tag{2.39}$$

3. **The inverse AC Josephson effect**
   By treating the junction with an ideal voltage bias of

   $$U(t) = U_0 + U_1 \cos \omega_1 t \tag{2.40}$$

and now integrating the 2.Josephson equation by time and inserting the phase difference in the first Josephson equation (and using the standard mathematical expansion of the sine of a sine in terms of Bessel funcions) yields [24]

$$\begin{aligned} \delta(t) &= \delta(0) + \omega_0 t + (2eU_1/\hbar\omega_1)\sin\omega_1 t & (2.41)\\ \omega_0 &\equiv 2eU_0/\hbar & (2.42)\\ I_s &= I_c \sum_{+\infty}^{n=-\infty} (-1)^n J_n\left(2eU_1/\hbar\omega_1\right)\sin\left(\delta(0) + \omega_0 t - n\omega_1 t\right) & (2.43) \end{aligned}$$

This contributes a DC component only when $\omega_0 = n\omega_1$, i.e. when the DC voltage U_0 has on of the *Shapiro step* values [22]: $U_n = n\hbar\omega_1/2e$.

As proposed this should yield a non-linear inductance. To extract this fact, one just derives the 1.Josephson equation by t and insert it into the first:

$$\begin{aligned} \frac{\partial I_s}{\partial t} &= I_c\cos(\delta)\frac{\partial\delta}{\partial t} & (2.44)\\ U(t) = \frac{\hbar}{2e}\frac{\partial\delta}{\partial t} &= \frac{\hbar}{2eI_c}\frac{1}{\cos\delta}\frac{\partial I_s}{\partial t} & (2.45) \end{aligned}$$

By comparing the last result with the induction law $U(t) = -L\frac{\partial I}{\partial t}$, the *Josephson inductance* L_j can be defined by

$$L_j \equiv \frac{\hbar}{2eI_c}\frac{1}{\cos\delta(t)} \tag{2.46}$$

The nonlinearity is given by the cosine-term of the phase difference. In a circuit diagram one draw the Josephson inductance as a cross, where the the the whole junction consists of an additional *Josephson capacitance* C_j. Imagine that initially at

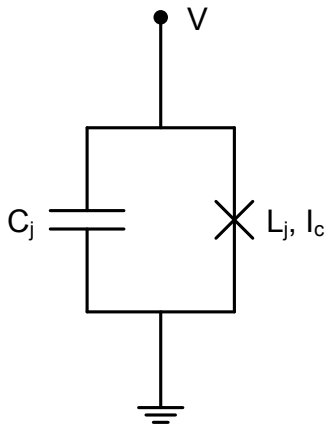

Figure 2.5: The Josephson junction as a circuit element.

time t=0 the junction was in the ground state, i.e. $\delta(t=0) = 0$ and finally at time

t the junction has the phase $\delta(t)$. So the junction energy is increased by

$$E_j = \int_0^t I_s U dt = \frac{\hbar}{2e} \int_0^t I_s \frac{\partial \delta(t)}{\partial t} dt = \frac{\hbar}{2e} \int_0^t I_c \sin(\delta)\, d\delta = \frac{I_c \hbar}{2e} (1 - \cos\delta) \quad (2.47)$$

Here $E_{j,0} \equiv \frac{I_c \hbar}{2e}$ sets the the characteristic scale of the Josephson energy and $(1 - \cos\delta)$ sets its dependence on the phase difference.

2.4 The Cooper pair box

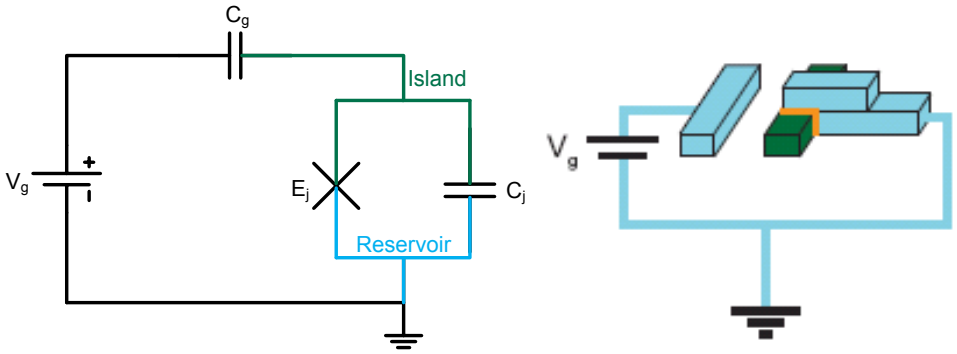

Figure 2.6: Left: Circuit diagram of a single CPB. Right: The superconducting island (dark green) is coupled to a superconducting reservoir via a Josephson tunnel junction (orange). A gate voltage is applied between the reservoir and the gate electrode.[19]

A single Cooper pair box consists of a small metallic island which is connected to a reservoir via a Josephson junction. In the superconducting state, the Cooper pairs are free to tunnel to and from the island, whose potential can be controlled by a gate voltage, V_g.[2] The behavior of the CPB is governed by two characteristic energies, the electrostatic charging energy, $E_C = e^2/2C_{tot}$ with $C_{tot} = C_j + C_g$ the total capacitance of the CPB and the Josephson energy, $E_j = \frac{I_c \hbar}{2e} \cos\delta$. Notice the neglect of the constant energy term $\frac{I_c \hbar}{2e}$ which occurred in equation 2.47 due to the integration, but this term can be set to zero by changing the lower integration limit, i.e. $\delta(t = 0) = \pm\pi/2$ so the wavefunctions of the two superconductors do not overlap in the initial state. The applied gate voltage induces a certain number of polarization charges n_g on one plate of the capacitor and thus the total charge on the island is given by $2e(n - n_g)$, where $n_g = C_g V_g / 2e$. This gate charges serves as a control parameter to change the number of Cooper pairs on the island, therefore the qubit is called *charged qubit*. The Hamiltonian of the Cooper pair box consists of an electrostatic

and a tunneling part

$$\begin{aligned}\hat{H}_{CPB} &= \hat{H}_{el} + \hat{H}_j && (2.48)\\ &= \frac{1}{2C_{tot}}\hat{Q}^2 - E_{j,0}\cos\hat{\delta}(t) && (2.49)\\ &= \frac{1}{2(C_j + C_g)}4e^2\left(\hat{n} - \hat{n}_g\right)^2 - E_{j,0}\cos\hat{\delta}(t) && (2.50)\end{aligned}$$

The first term of the CPB Hamiltonian represents the energy of a capacitor with a fixed, integer-quantized charge. The Josephson term $\hat{H}_j$ on the other hand describes the coherent tunneling of Copper pairs onto the superconducting island, where $E_{j,0}$ is the energy required for such a transfer of a Cooper pair from the reservoir to the island and $\hat{H}_j$ can then be considered as a discrete kinetic energy term of the tunneling process.[7] To find the eigenstates of the Hamiltonian, one has to define a complete basis for all states of the CPB, it's quite obvious to choose the charge basis which is defined by the number operator of the Cooper pairs on the island, i.e.

$$\begin{aligned}\hat{n}\left|n\right\rangle &= n\left|n\right\rangle && (2.51)\\ I &= \sum_n \left|n\right\rangle\left\langle n\right| && (2.52)\\ \left\langle m|n\right\rangle &= \delta_{mn} && (2.53)\end{aligned}$$

To rewrite the CPB Hamiltonian into this basis, it's necessary to transform the conjugate variable $\hat{\delta}$ into the charge basis. This can be done by using $\cos\hat{\delta} = (exp(i\delta) + exp(-i\delta))/2$ and $[\hat{\delta}, \hat{n}] = i$

$$\begin{aligned}\hat{H}_{CPB} &= \sum_n \left(4E_{C,0}(\hat{n} - \hat{n}_g)^2|n\rangle\langle n| - \frac{E_{j,0}}{2}\left(|n\rangle\langle n+1| + |n+1\rangle\langle n|\right)\right) && (2.54)\\ E_{C,0} &\equiv \frac{e^2}{2C_{tot}} && (2.55)\end{aligned}$$

In the charge basis, the Schroedinger equation of the CPB can only be solved numerically.

The shape of the energy bands can be expressed in terms of the gate charge n_g as shown in figure 2.7. The diagonal elements of the Hamiltonian in the charge basis are parabolic in n_g, i.e. $4E_{C,0}(\hat{n} - \hat{n}_g)^2$, and have a periodicity of 2e. Degeneracy occurs at the crossing point of this energy parabolas. This so-called *charge degeneracy points* are abolished by the off-diagonal matrix elements of the second term in the Hamiltonian. Perturbation leads to a coupling of the charge eigenstates $|n\rangle$ and $|n+1\rangle$ which has an energy difference of E_j at the degeneracy point, i.e. $n_g = odd$. Now we can also see the non-linear energy differences between the charge eigenstates, which is due to the non-linear Josephson inductance. The possibility of realizing an

anharmonicity in the energy diagram makes it possible to treat the CPB as a to level system.

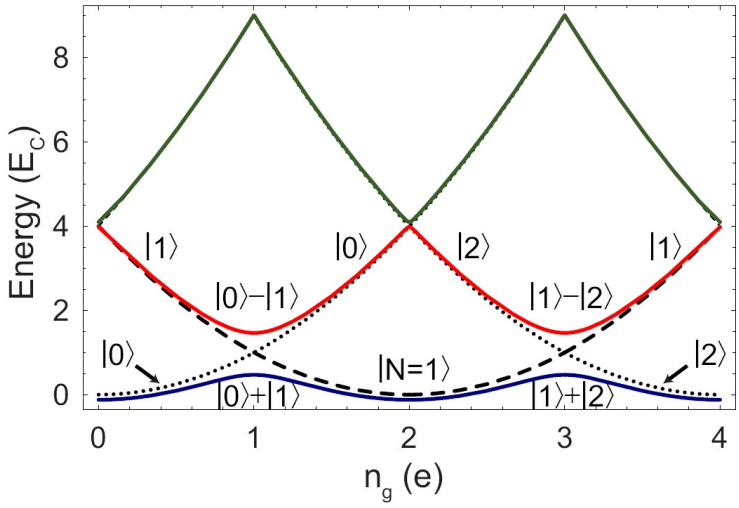

Figure 2.7: CPB energy levels. Dotted and dashed black lines show electrostatic energy of island for 0 and 1 Cooper pairs present on the island. The blue, red, and green solid bands show the ground, and the first two excited state energy levels. At $n_g = 1$ there is an avoided crossing, where the eigenstates are superpositions of n and n + 1 Cooper pairs.[19]

2.5 Split CPB

In the last section, one applied a gate voltage to tune the electrostatic energy ($\hat{H}_{el}$). But it is also possible to tune the tunneling component of the Hamiltonian ($\hat{H}_j$). This can be done by splitting the Josephson junction, as shown in Figure 2.8. Each

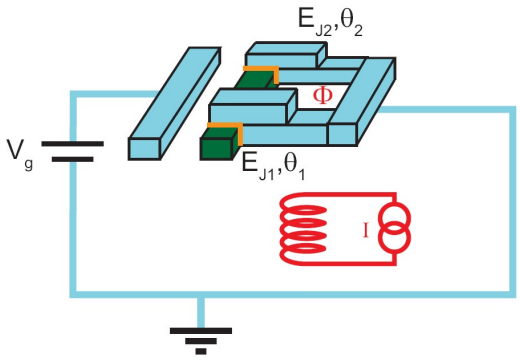

Figure 2.8: Schematic draw of a split Cooper pair box, where the island is now connected with two Josephson junctions with different Josephson energies, labeled by E_{j1}, E_{j2}. With an additional external magnetic flux Φ one can tune this characteristic energies.[19]

Josephson junction has a characteristic tunneling energy E_{j1}, E_{j2} and also different phase differences Θ_1, Θ_2. By adding this second split CPB to the tunneling part of the Hamiltonian one get

$$\hat{H}_j = E_{j1} \cos \hat{\Theta}_1 + E_{j2} \cos \hat{\Theta}_2 \tag{2.56}$$

Introducing the following new variables

$$\hat{\Theta} \equiv \frac{\hat{\Theta}_1 + \hat{\Theta}_2}{2} \tag{2.57}$$

$$\hat{\beta} \equiv \hat{\Theta}_1 - \hat{\Theta}_2 \tag{2.58}$$

It can be shown by calculating the free energy density in the Ginzburg-Landau-Approximation and using Stokes-Theorem that the global phase difference operator $\hat{\beta}$ can be expressed in terms of the magnetic flux through the loop[24]

$$\hat{\beta} = 2\pi\Phi/\Phi_0 \tag{2.59}$$

where $\Phi_0 \equiv h/2e$ is called the *flux quantum*. Now, rewriting $\hat{H}_j$ by using some trigonometric substitutions

$$\hat{H}_j = (E_{j1} + E_{j2}) \cos\left(\pi \frac{\Phi}{\Phi_0}\right) \cos \hat{\Theta} + (E_{j1} - E_{j2}) \sin\left(\pi \frac{\Phi}{\Phi_0}\right) \sin \hat{\Theta} \tag{2.60}$$

If the two junctions are symmetric, i.e. $E_{j1} = E_{j2}$, or if there is no external flux, i.e. $\Phi = 0$, the expression simplifies to

$$E_{j1} = E_{j2}: \qquad \hat{H}_j = 2E_{j1} \cos\left(\pi \frac{\Phi}{\Phi_0}\right) \cos \hat{\Theta} \tag{2.61}$$

$$\Phi = 0: \qquad \hat{H}_j = (E_{j1} + E_{j2}) \cos \hat{\Theta} \tag{2.62}$$

So, for identical Josephson junctions, the tunneling energy is periodical in the external magnetic flux (periodicity given by $\Phi = 2n\Phi_0$). And if no external flux is applied, one can observe the well known behavior.

2.6 Transmon

The CPB is quite sensitive to fluctuations of the gate charge n_g as one can see in Fig.2.7. It's therefore desirable to have an energy diagram which is not that sensitive, i.e. the shape of the energy versus gate charge should be more flatten for the ground and first excited state. This will yield a much more immune qubit frequency to charge noise. It can be achieved by enlarging the total capacitance between the island and the reservoir. This lead to a much larger linearity of the CPB as shown in Fig. 2.9

These improved Cooper pair boxes are called *Transmons*. As shown in Figure 2.10,

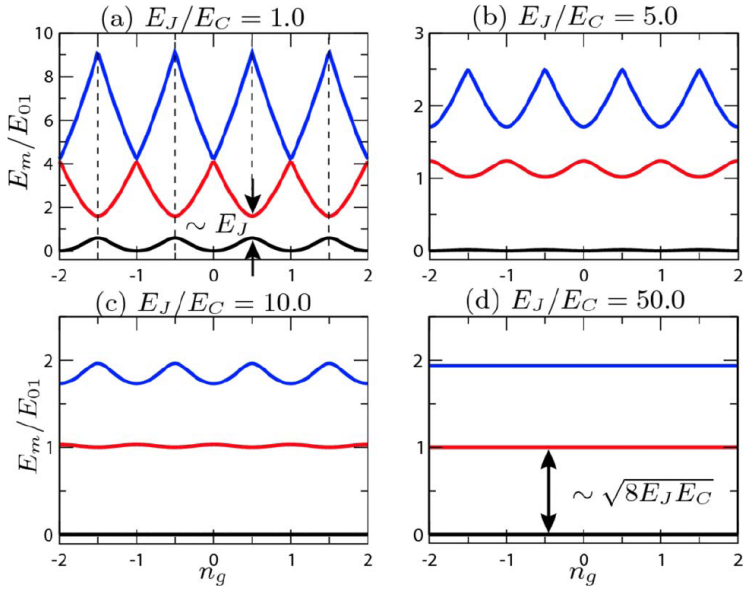

Figure 2.9: CPB energy bands at different E_j/E_C ratios. As the ratio is increased one can immunizing the CPB to charge fluctuations. A side effect is that anharmonicity is also reduced.[11]

the parallel capacitor C_B is realized with a finger liker structure.

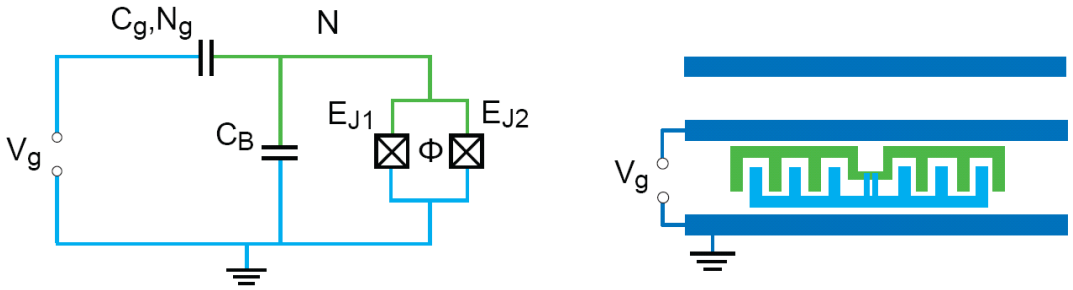

Figure 2.10: Reduced circuit diagram and sketch of a transmon capacitively coupled to a transmission line resonator[7]

2.7 Microwave cavity

So far, the artificial atom which is realized in cQED by a Transmon has been discussed. To excite and read out the qubit one has to couple this Transmon to a photon in a cavity. In typical experiments, a single mode of an electromagnetic field is trapped between two mirrors with a high reflectivity such that it can be considered as a standing wave. Remember the second quantization of the elm field yields again a

description like the harmonic oscillator in quantum mechanics. In this section the photon cavity would be analysed.

2.7.1 The lumped-element circuit model for a transmission line

To develop a differential equation for the voltage and the current through a two-wire line we want to look at an infinitesimal short piece of line, which can be modeled as a lumped-element circuit: where

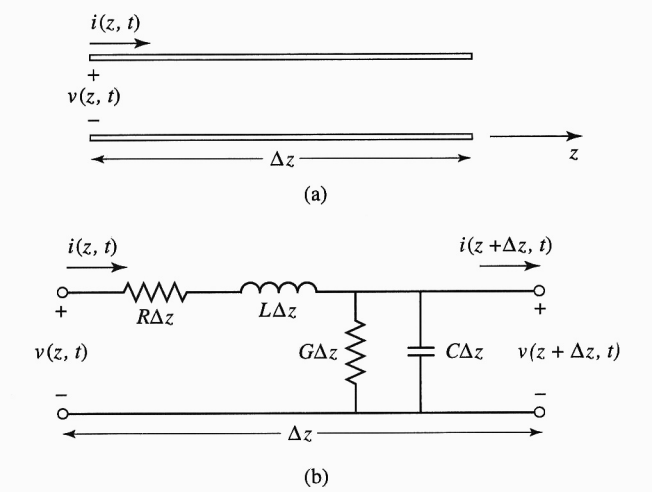

Figure 2.11: Voltage and current definitions and equivalent circuit diagram for an incremental length of transmission line.[18]

R = series resistance per unit length, for both conductors, in Ω/m
L = series inductance per unit length, for both conductors, in H/m
G = shunt conductance per unit length, in Ω^{-1}/m
C = shunt capacitance per unit length due to the close proximity of the two conductors, in F/m.

G describes the dielectric loss in the material between the conductors.
The characteristic impedance Z_0 is defined by

$$Z_0 = \frac{V_0^+}{I_0^+} = \frac{-V_0^-}{I_0^-} \tag{2.63}$$

We find the general solution

$$v(z,t) = V_0^+ e^{-\gamma z + i\omega t} + V_0^- e^{\gamma z + i\omega t} \quad (2.64)$$

$$i(z,t) = \frac{V_0^+}{Z_0} e^{-\gamma z + i\omega t} - \frac{V_0^-}{Z_0} e^{\gamma z + i\omega t} \quad (2.65)$$

$$Z_0 = \frac{R + i\omega L}{\gamma} = \sqrt{\frac{R + i\omega L}{G + i\omega C}} \quad (2.66)$$

$$\gamma = \alpha + i\beta = \sqrt{(R + i\omega L)(G + i\omega C)} \quad (2.67)$$

It has the same form as a plane wave in a lossy medium, where α describes the rate of decay. With this similarity we can define a wavelength λ and a phase velocity v_p

$$\lambda = \frac{2\pi}{\beta} \quad (2.68)$$

$$v_p = \frac{\omega}{\beta} = \lambda\omega/2\pi \quad (2.69)$$

The lossless line fulfills the condition R=G=0.

2.7.2 Conventional coplanar waveguide

A coplanar waveguide (CPW) consists of a dielectric substrate with conductors on the top surface. The conductors formed a center strip separated by a narrow gap from two ground planes on either side. If we know the dimensions of the center strip, the gap, the thickness and permittivity of the dielectric substrate we can calculate the effective dielectric constant ϵ_{eff}, characteristic impedance Z_0 and the attenuation α of the line.

Conductor-backed coplanar waveguide

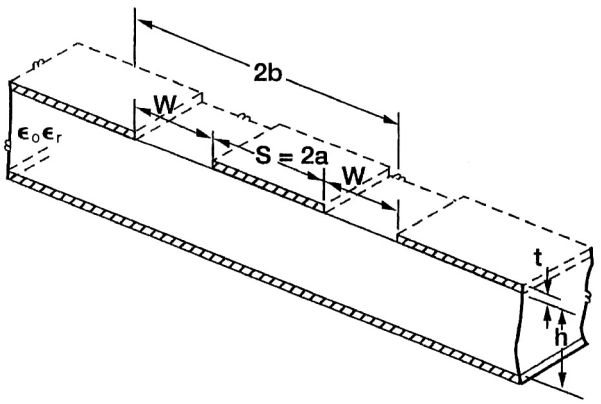

Figure 2.12: Schematic of conductor backed coplanar waveguide (CBCPW).[21]

This is just a coplanar waveguide with a lower ground plate as shown in figure (2.12). The lower ground plane provides mechanical strength for a thin and fragile wafer and acts as a heat sink for circuits with active devices. Such a waveguide is called *conductor-backed coplanar waveguide*, short CBCPW. The characteristic impedance is determined by the ratio of a/b, the substrate height h and the dielectric constant of the substrate ϵ_r

$$Z_0^{CPW} = \frac{60\pi}{\sqrt{\epsilon_{eff}}} \cdot \frac{1}{\frac{K(k)}{K(k')} + \frac{K(k_3)}{K(k_3')}} \tag{2.70}$$

where the effective dielectric constant is given by

$$\begin{aligned}
\epsilon_{eff} &= \frac{1 + \epsilon_r \widetilde{K}}{1 + \widetilde{K}} && (2.71)\\
\widetilde{K} &= \frac{K(k')K(k_3)}{K(k)K(k_3')} && (2.72)\\
k &= a/b && (2.73)\\
k_3 &= \frac{\tanh(\frac{\pi a}{2h})}{\tanh(\frac{\pi b}{2h})} && (2.74)\\
k' &= \sqrt{1-k^2} && (2.75)\\
k_3' &= \sqrt{1-k_3^2} && (2.76)
\end{aligned}$$

where K is the complete elliptic integral of the first kind, i.e.

$$K(m) := \int_0^{\pi/2} (1 - m \cdot \sin^2\Theta)^{-1/2}\, d\Theta \tag{2.77}$$

Notice that in our case $h \ll a, b$ and we can therefore do the approximation $k_3 \approx a/b = k$ and also $k' \approx k_3'$ which leads to $\epsilon_{eff} \approx \frac{1+\epsilon_r}{2}$.

2.7.3 parallel RLC resonant circuit

If we cut the CPW such that two equal gaps arise, we have a resonator which is capacitive coupled to the input and output waveguides. The gap capacitors is then in accordance with the mirros to trap the electromagnetic wave. Near its resonance frequency it can be modeled by a parallel RLC resonant circuit. Firstly, a parallel RLC resonator will be discussed. Figure (2.13) a) shows a RLC resonator.

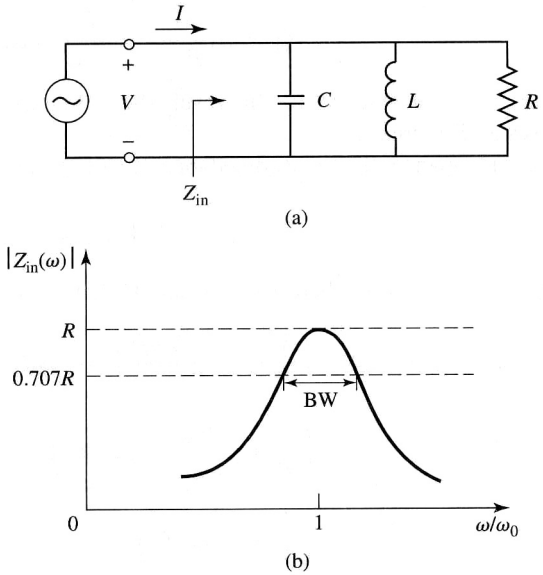

Figure 2.13: A parallel RLC resonator and its response. (a) The parallel RLC circuit. (b) The input impedance magnitude versus frequency.

The input impedance is given by

$$Z_{in} = \left(\frac{1}{R} + \frac{1}{i\omega L} + i\omega C\right)^{-1} \tag{2.78}$$

which is dependent on ω as shown in figure (2.13) b).
As for the LC-oscillator, one has the same resonant frequency which is independent of the resistance

$$\omega_0 = \frac{1}{\sqrt{LC}} \tag{2.79}$$

Another important parameter of a resonant circuit is its quality factor Q, which is defined as

$$Q(\omega) = \omega \cdot \frac{\text{(average energy stored)}}{\text{(energy loss per second)}} \tag{2.80}$$

Thus, $Q(\omega)$ is a measure of the loss of a resonant circuit, i.e. lower loss implies a higher quality factor.
At $\omega = \omega_0$

$$Q(\omega_0) = \omega_0 RC \tag{2.81}$$

This result shows that the Q of a parallel resonant circuit increases as R increases.
Near the resonance frequency, the input impedance can be simplified by using $\omega =$

$\omega_0 + \Delta\omega$ where $\Delta\omega$ is small compared to ω_0

$$Z_{in} \approx \frac{R}{1 + 2i\Delta\omega RC} = \frac{R}{1 + 2iQ\Delta\omega/\omega_0} \tag{2.82}$$

When $R \to \infty$ we can write near the resonance

$$Z_{in} = \frac{1}{2iC\left(\omega - \omega_0\right)} \tag{2.83}$$

The effect of loss can be accounted by replacing ω_0

$$\omega_0 \to \omega_0 \cdot \left(1 + \frac{i}{2Q}\right) \tag{2.84}$$

A resonator with loss can therefore be modeled as a lossless resonator whose resonant frequency ω_0 has been replaced by a complex effective resonant frequency.
The half-power bandwidth occurs when the real part of $P_{in} = |V|^2|Z_{in}|^{-1}/2$ is half of the maximum

$$|Z_{in}|^2 = \frac{R^2}{2} \tag{2.85}$$

which, from (2.82), implies

$$\text{bandwidth (BW)} = \frac{1}{Q} \tag{2.86}$$

see figure (2.13) b).

2.7.4 Loaded and unloaded Q

The quality factor Q is a characteristic of the resonant circuit itself in the absence of any loading effects caused by external circuits and so it is called the unloaded Q. But often, a resonant circuit is coupled to an other external circuit. Figure (2.14) shows a resonator coupled to an external load resistor R_L. If the resonator is a parallel RLC

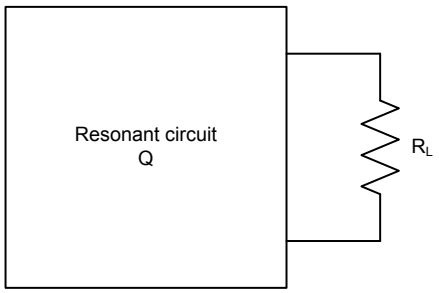

Figure 2.14: A resonant circuit connected to an external load, R_L

circuit, the load resistor R_L combines with R so that the effective resistance is $\frac{RR_L}{R+R_L}$. We can define an external quality factor Q_e as

$$Q_e = \frac{R_L}{\omega_0 L} \tag{2.87}$$

then the loaded Q_L can be expressed as

$$\frac{1}{Q_L} = \frac{1}{Q_e} + \frac{1}{Q} \tag{2.88}$$

In the measurement the loaded Q_L of the resonator is determined. The unloaded quality factor Q is given by

$$Q = \frac{Q_L}{1 - 10^{-L_0/20}} \tag{2.89}$$

where L_0 is the insertion loss.[28][26]

2.7.5 Open-Circuited $\lambda/2$ Line

As mentioned in chapter (2.7.3) the gaps in a CPW cause a capacitive coupling and therefore build a microwave resonator. Near its resonance frequency ω_0, such a resonator will behave as a parallel RLC resonator, when the length of the open-circuited transmission line is $\lambda/2$, or multiples of $\lambda/2$. Consider a lossy transmission line of given length l, which has a characteristic impedance Z_0 , propagation constant β, and an attenuation constant α. The relation between the RLC circuit and the

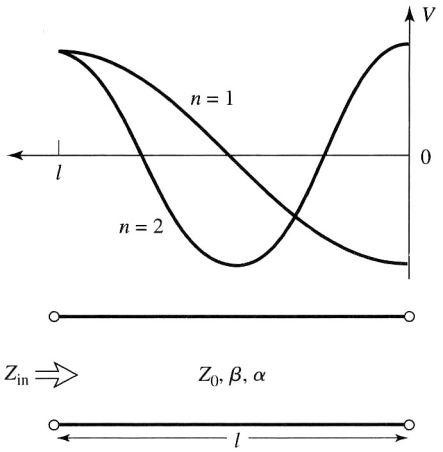

Figure 2.15: An open-circuited length of lossy line, and the voltage distributions for $n = 1$ ($\lambda/2$) and $n = 2$ ($l = \lambda$) resonators

open-circuited $\lambda/2$ line can be expressed as

$$R = \frac{Z_0}{\alpha l} \tag{2.90}$$

$$C = \frac{\pi}{2\omega_0 Z_0} \tag{2.91}$$

$$L = \frac{1}{\omega_0^2 C} \tag{2.92}$$

$$Q = \omega_0 RC = \frac{\pi}{2\alpha l} = \frac{\beta}{2\alpha} \tag{2.93}$$

since $l = \frac{\pi}{\beta}$ at resonance. Where the left-hand side of the equations are the parameters of the RLC circuit.

2.7.6 Capacitive coupling

The open-circuited $\lambda/2$ line is just connected to the other transmission line by a gap which can be described as a capacitive coupling. We have first to calculate the external quality factor Q_e due to the series $R_L C_g$-circuit which couples to the resonator. At the resonant frequency

$$Q_e \equiv Q_e(\omega_0) = \frac{\pi}{4Z_0} \cdot \frac{1 + R_L^2 \omega_0^2 C_g^2}{R_L \omega_0^2 C_g^2} \tag{2.94}$$

Now the loaded quality factor of the resonator, Q_L, is found

$$\frac{1}{Q_L} = \frac{1}{Q_e} + \frac{1}{Q} \tag{2.95}$$

where $Q = R\pi/(4Z_0)$
It is useful to define a coefficient of coupling, g, as

$$g = \frac{Q}{Q_e} \tag{2.96}$$

Then, three cases can be disinguished

1. $g < 1$ The resonator is said to be undercoupled to the feedline
2. $g = 1$ The resonator is critically coupled to the feedline
3. $g > 1$ The resonator is said to be overcoupled to the feedline

To obtain maximum power transfer between a resonator and a feedline, the resonator must be matched to the feed at the resonant frequency, this occurs when

$$C_{g,crit} = \frac{1}{\omega_0} \cdot \frac{1}{\sqrt{2Z_0 R R_L - R_L^2}} \tag{2.97}$$

2.8 Circuit QED

As discussed in the previous sections, the Cooper pair box respectively the Transmon can be treated as an artificial atom (2-level system) which can then be coupled to a transmission line resonator to control and read out the qubit state. In this chapter the interaction between the atom and the radiation field will be discussed on a fully quantum mechanical level. Therefore, the hats on top of the operators will be neglected.

2.8.1 Cavity quantum electrodynamics

The interaction between the two-level atom and a harmonic oscillator whose excitations are photons is described by the *Jaynes-Cummings Hamiltonian*[27]:

$$H_{JC} = \hbar\omega_r(a^+a + 1/2) + \hbar\frac{\omega_a}{2}\sigma_z + \hbar g(a^+\sigma^- + a\sigma^+) + H_\kappa + H_\gamma \tag{2.98}$$

where the first term represents the energy of the electromagnetic field, each photon contains an energy $\hbar\omega_r$ which is also twice the zero energy level. The second term represents the atom as 2-level system with a transition energy $\hbar\omega_a$. The third term describes a dipole interaction where the artificial atom can absorb ($a\sigma^+$) and emit ($a^+\sigma^-$) a photon from/to the field at rate g. These three terms describe the coherent dynamics, whereas the last two terms describe decoherence effects, where H_κ stands for the energy losses due to the cavity decay rate $\kappa = \omega_r/Q$ depending on the quality factor of the transmission line resonator. The second loss effect happens by the coupling of the atom to other modes of the electromagnetic field which therefore causes a decoherence of the excited state, given by the decay rate γ.

When the cavity and atom frequencies are degenerate, i.e. $\omega_a = \omega_r$, the eigenstates of the Jaynes-Cummings Hamiltonian in absence of the last two decoherence effects are the entangled states between the atom and the field $|\phi_\pm\rangle = (|\downarrow, n\rangle \pm |\uparrow, n-1\rangle)/\sqrt{2}$. An initial state where the atom is in the excited state and n photons are in the cavity therefore decays into the ground state and with one less photon, this process is then reversed such that this transition occurs at the *vacuum Rabi frequency* g/π. The entangled state decays at a rate of $(\kappa + \gamma)/2$. The energies of these new states are split by $2g\sqrt{n}$ and is therefore not linear in the photon number, see Figure 2.17 left. When many oscillations can be completed before the atom decays or the photon gets lost, the system is then in the strong coupling limit of cQED, i.e. $g > \kappa\gamma, 1/T_{trans}$.[3] By detuning the atom and the cavity by $\Delta = \omega_a - \omega_r$, where $g << \Delta$ one reaches the so-called *dispersive limit*. In this limit, the Jaynes-Cummings Hamiltonian can be approximated using perturbation theory.[3] Expanding in powers of g/Δ to second

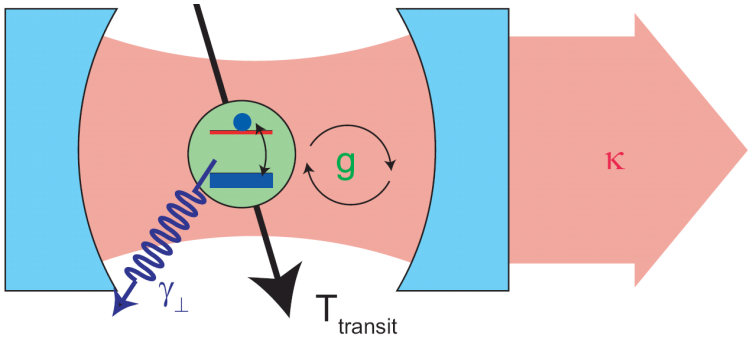

Figure 2.16: A two level atom interacts with the field inside cavity with highly reflective mirrors, i.e. a large quality factor. The atom coherently interacts with the cavity at a rage g. Also visible: The photon decay rate κ out of the cavity and the atom decay rate γ into other field modes. The rate at which the atom leaves the cavity, $1/T_{transit}$ is not relevant for cQED. To reach the strong coupling limit, the interaction rate must be larger than the rates of decoherence $g > \kappa, \gamma, 1/T_{transit}$. [19]

order yields

$$H_{JC} \approx \hbar \left(\omega_r + \frac{g^2}{\Delta} \sigma_z \right) a^+ a + \frac{\hbar}{2} \left(\omega_a + \frac{g^2}{\Delta} \right) \sigma_z \tag{2.99}$$

As one can see, the energies of the atom and the photons are shifted. The first term remains the Hamiltonian of the harmonic oscillator, but the frequency is shifted by g^2/Δ and also depends on the state of the atom, as we will see later, this can be used to readout the qubit state without demolition of its state. The second term shifts the atom transition frequency by the amount of g^2/Δ and is called *Lamb shift*[8]. It means that the photons which are used to measure the state of the atom will also be modified, due to the Heisenberg uncertainty principle, but neither the state of the atom nor the of the photon will be destroyed. Such a measurement is called *Quantum Non-demolition measurement*, QND, which preserves the integrity of the system and the value of the measured observable. This allows to measures the same system repeatedly, but it does not imply that the wave function fails to collapse, it's just the ideal quantum projective measurement.[13]
By rewriting the Hamiltonian in the dispersive limit by leaving the electromagnetic field unaffected one gets

$$H_{JC} \approx \hbar\omega_r (a^+ a + 1/2) + \frac{\hbar}{2} \left(\omega_a + \frac{2g^2}{\Delta} a^+ a + \frac{g^2}{\Delta} \right) \sigma_z \tag{2.100}$$

Such that a photon number-dependent *Stark shift*[19], $2ng^2/\Delta$ and again the vacuum noise induced Lamb shift, g^2/Δ occurs to the atom transition frequency.

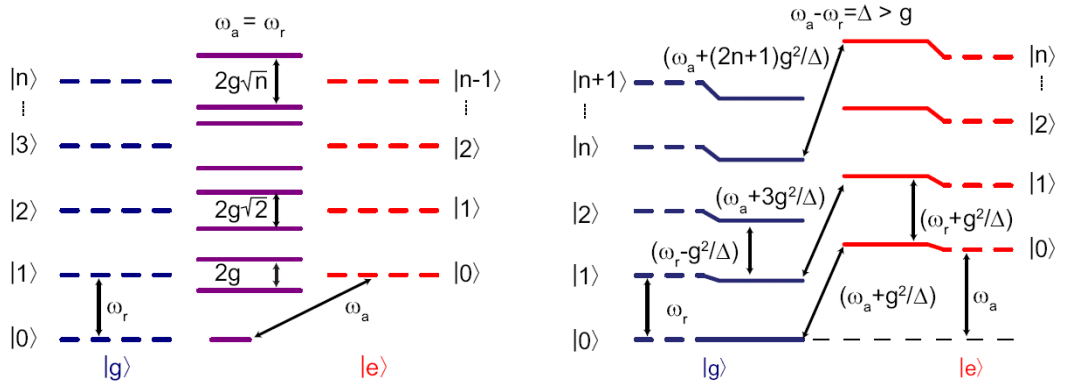

Figure 2.17: Energy level diagrams of the Jaynes-Cummings Hamiltonian. The dashed lines are the eigenstates of the uncoupled Hamiltonian, where $|g\rangle$ respectively $|e\rangle$ correspond to the ground/excited state of the atom and $|n\rangle$ describes the photon number inside the cavity. The solid line then represents the eigenstates of the coupled system. a) Resonant case, i.e. $\omega_a - \omega_r << g$. Eigenstates are then a symmetric and antisysmmetric entanglement of the uncoupled atom and the resonator mode. Notice the photon number square-root dependence of the splitting. b) Dispersive limit , $\omega_a - \omega_r >> g$ of the Jaynes-Cummings Hamiltonian. Frequency shift of the resonator and the atom transition frequency due to the Heisenberg uncertainty principle which can be used to do a Quantum Non-Demolition Measurement (QND).[19]

2.8.2 Coupling the CPB to the cavity

The circuit QED system consists of the coplanar microwave resonator of length L with its standing wave (electrical component shown in Figure 2.18) and the integrated, superconducting qubit which is located between the resonator line and the ground plane. To reach a maximal coupling between them, the CPB is positioned near an antinode of the field. The island of the CPB is therefore positioned near the center conductor of the resonator, which acts as a gate electrode for the Cooper pairs tunneling between the island and the reservoir. This allows to apply a DC voltage at the center conductor of the resonator via capacitive coupling over the input gap capacitance and therefore apply a gate voltage V_{DC} to the CPB via the capacitance between the center conductor and the island. Another parameter is the external magnetic field which induces a flux through the split CPB and therefore tune the tunneling energy (E_j). One can regard the Josephson energy E_J gained when a Cooper pair tunnels through the tunnel barrier (about 1 nm thick).
The total voltage can be written as the sum of the classical DC voltage and a quantum voltage due to the photons inside the resonator.

$$V_g = V_{DC} + \hat{V} \tag{2.101}$$

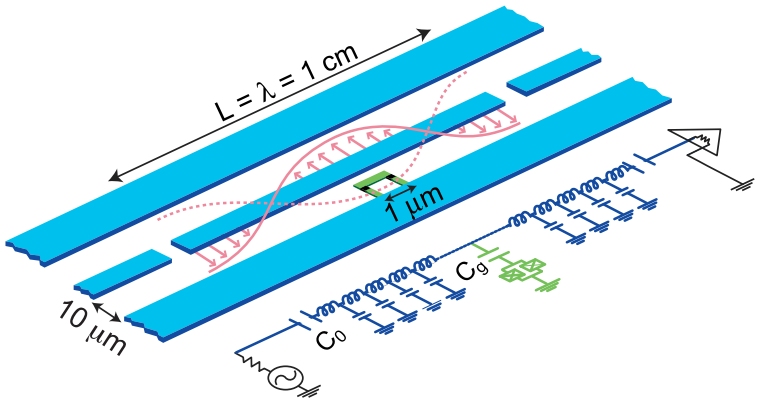

Figure 2.18: Schematic layout and equivalent lumped circuit representation of the implementation of cavity QED using superconducting circuits.[3]

where $\hat{V} = \hat{Q}/C$, compare to equation 2.27. This leads to

$$\hat{V} = \sqrt{\frac{\hbar\omega_r}{2C}}(a + a^+) \equiv V_0(a + a^+) \tag{2.102}$$

with V_0 indicates the rms of the vacuum fluctuations. By inserting this into the electrostatic part of the CPB-Hamiltonian (equation 2.48) one can find the capacitive coupling strength between the qubit and the resonator

$$H_{coup} = 2\hbar g(a^+ + a)\hat{n} \tag{2.103}$$

$$g = \frac{eV_0}{\hbar}\eta \tag{2.104}$$

$$\eta = C_g/C_{tot} \tag{2.105}$$

The corresponding voltage of the vacuum fluctuations can easily be derived by the zero point energy of the resonator, i.e. $\hbar\omega_r/2$ where half of this value is stored in the electrical field and can be identified by a voltage

$$\frac{1}{2}\left(\frac{1}{2}\hbar\omega_r\right) = \frac{1}{2C}V_0^2 \tag{2.106}$$

The coupling constant $2\hbar g$ can be seen as the energy in moving a Cooper pair across the portion of the rms vacuum voltage fluctuations, V_0, in the resonator.
Let's assume $n_g = 1$ where the CPB is usually operated and the number operator of the Cooper pairs on the island can be written as $\hat{n} = X/2$ (X is the Pauli matrix given in 2.6). By making the rotating wave approximation which neglect higher frequency terms of the form $\omega_r + \omega_a$ and is a valid approximation when the applied electromagnetic radiation is near resonance with the qubit transition frequency, and

the intensity is low

$$(a^+ + a)X \approx a^+\sigma^- + a\sigma^+ \tag{2.107}$$

In the charge basis, this approximation ignores terms like $a^+\sigma^+$ and $a\sigma^-$ which would change the number of excitations in the whole system (photons and qubit). The coupling Hamiltonian the yields the already defined term in equation 2.98.

$$H_{coup} = \hbar g(a^+\sigma^- + a\sigma^+) \tag{2.108}$$

2.8.3 Readout Scheme

In the dispersive limit, where no photons are absorbed by the atom, which can be achieved by detuning the atom and cavity much larger than g, i.e. $\Delta > g$, one can observe a photon number dependent frequency shift of the atom and a qubit state dependent frequency shift of the light inside the resonator. This second shift of the resonator spectrum, $\omega_r \approx \omega_r \pm g^2/\Delta$, where $\Delta = |\omega_a - \omega_r|$ is the detuning, provides the possibility to probe the qubit state by measuring the phase and the intensity of the transmitted microwave. The phase shift is expected to be [3] $\arctan(2g^2/\kappa\Delta)$. A necessary condition in order to be able to resolve the states nicely is that $\kappa \approx 2g^2/\Delta$ or smaller, which means that the linewidth of the resonator has to be at least in the order of the frequency shift that arises when the qubit changes its state.

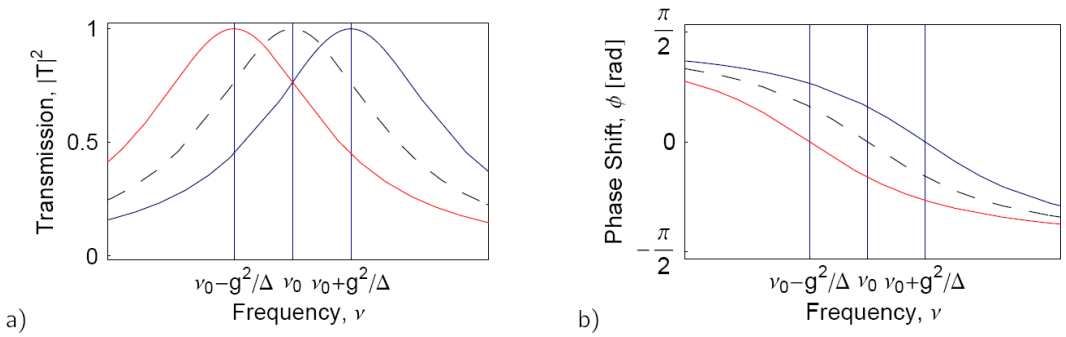

Figure 2.19: a) Amplitude and b) phase of the transmission spectrum of the cavity for the ground (red) and excited (blue) qubit state. Dashed line represents the bare resonant frequency.[6]

2.8.4 Sideband transitions

The general solutions of the Jaynes-Cumming Hamiltonian (equation 2.98) in absence of the damping term, i.e. H_κ and H_γ, are given by the so-called *dressed states* [3]

$$|\overline{+,n}\rangle = \cos\Theta_n|e,n\rangle + \sin\Theta_n|g,n+1\rangle \quad (2.109)$$

$$|\overline{-,n}\rangle = -\sin\Theta_n|e,n\rangle + \cos\Theta_n|g,n+1\rangle \quad (2.110)$$

$$\Theta_n \equiv \frac{1}{2}\arctan\left(\frac{2g\sqrt{n+1}}{\Delta}\right) \quad (2.111)$$

$$\Delta \equiv \omega_a - \omega_r \quad (2.112)$$

The ground state of this Hamiltonian is $|g,n\rangle$ with corresponding eigenenergies

$$E_{\overline{\pm,n}} = (n+1)\hbar\omega_r \pm \frac{\hbar}{2}\sqrt{4g^2(n+1)+\Delta^2} \quad (2.113)$$

$$E_{g,0} = -\frac{\hbar\Delta}{2} \quad (2.114)$$

Figure2.17 shows the corresponding energy diagram for two different detuning regimes. To see which transitions are allowed, one has to look at the behavior of the parity operator $P = \sum_{n=0}^{\infty}(-1)^n|n\rangle\langle n|\sigma_z$ acting on this eigenstates:

$$P|g,0\rangle = -|g,0\rangle \quad (2.115)$$

$$P|\overline{\pm,n}\rangle = (-1)^n|\overline{\pm,n}\rangle \quad (2.116)$$

The selection rule now only allows transitions between states of different parity. To show this one has to calculate the dipole matrix element of to states with the same parity[9]

$$D_{12} = \int d^3r\Psi_2^*(\vec{r})[e\vec{r}]\Psi_1(\vec{r}) \quad (2.117)$$

By substitute $\vec{r}' \equiv -\vec{r}$, which has the same effect as the parity operator acting on them, yields the negative value

$$D_{12} = \int d^3r'\Psi_2^*(-\vec{r}')[e(-\vec{r}')]\Psi_1(-\vec{r}') \quad (2.118)$$

$$= -\int d^2r'\left[\pm\Psi_2^*(\vec{r}')\right][e\vec{r}']\left[\pm\Psi_1(\vec{r}')\right] \quad (2.119)$$

$$= -D_{12} \quad (2.120)$$

this can only be valid for $D_{12} = 0$.
At the charge degeneracy point the dipole moment is given by [3] $d = \hbar g/\epsilon_{rms}$, where ϵ_{rms} is the electric field which correspond to the rms vacuum voltage fluctuations, V_0 and is about $2 \cdot 10^4 e a_0$. A transition between $|g,0\rangle$ and $|g,1\rangle$ (blue sideband) is

therefore forbidden to first order in the dispersive limit, $\Delta >> g$. In the same way, a transition between $|g,1\rangle$ and $|e,0\rangle$ (red sideband) is not allowed in the dispersive limit. But it's possible to reach this transition with 2 photons driving it.

In the dispersive regime as already discussed, the qubit and the resonator do not directly exchange energy but the residual dispersive coupling still allows sideband transitions linking the qubit and resonator states by driving it with a strong additional microwave.[12]

The so-called *blue sideband* transition involves the simultaneous excitation of the qubit by also adding a photon, this occurs at a transition frequency of $\omega_A^+ = \omega_r + \omega_A$, while the *red sideband* is the transition between the states $|g1\rangle \leftrightarrow |e0\rangle$ with frequency $\omega_A^- = |\omega_r - \omega_A|$, see Figure 2.20. This sideband transitions can only be driven by 2 photons, here we choose to drive the blue sideband with 2 photons of equal energy whereby only one signal generator is necessary. In this configuration the drive is equally detuned from the qubit and the resonator, such that undesired offresonant driving of the bare qubit transition and off-resonant population of the resonator would occur at the same rate.

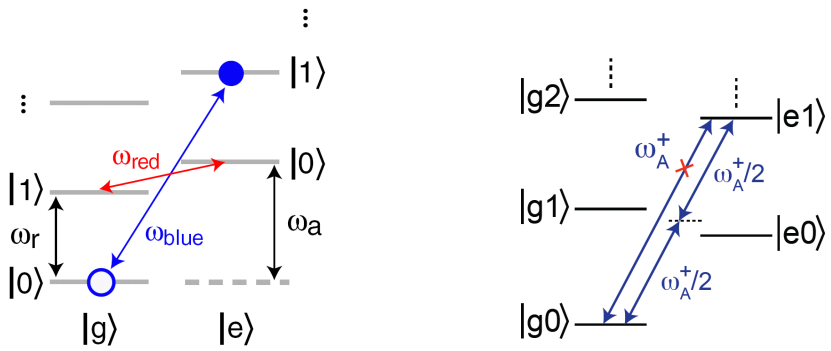

Figure 2.20: Left: Dispersive dressed states energy level diagram. Red and blue sideband transitions are indicated.[25] Right: Combined level diagram for the blue sideband transition, which is forbidden to first order, but may be driven using two photons.[12]

3 IQ-mixer calibration for accurate pulse shaping

An IQ-mixer consists of two balanced mixers and two hybrids. One hybrid is a so called *quadrature hybrid*, which is a 3 dB directional coupler with a 90 degree phase difference in the outputs. Figure 3.1 shows the circuit diagram of a 90 degree hybrid, where the input signal is on port 1 and is then evenly divided between ports 2 and 3, with a 90 degree phase shift. Port 4 is the isolation port. Observe that this hybrid is highly symmetric such that any port can be used as the input port. The second

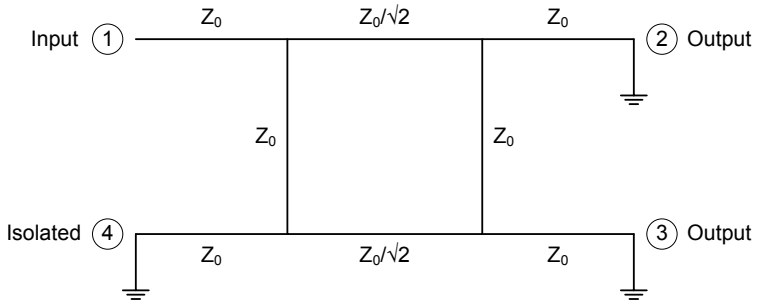

Figure 3.1: Circuit of the quadrature hybrid.

hybrid just acts as a directional coupler and can be realized by a T-junction. A circuit diagram for a double balanced mixer is shown in Fig. 3.2. Both the LO and RF ports are balanced and all ports of the mixer are inherently isolated from each other. Depending on the the sign of the LO-Signal, either the diodes D_1 and D_4 or the diodes D_2 and D_3 let pass the signal. This switching between the two different path is the fundamental principle of a mixer. A detailed analysis of this process can be found in reference [18].

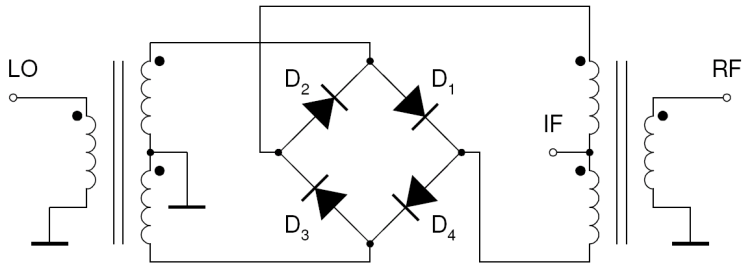

Figure 3.2: Block diagram of a double balanced mixer.

In our settings (up-converter) it should provide one RF (Radio Frequency) signal at the frequency $f_{LO} - f_{IF}$, but in the uncalibrated case it leads to two RF signals at $f_{LO} \pm f_{IF}$ which are 2 times the IF (Intermediate Frequency) apart in the frequency-space with different powers. We need this mixers to generate modulated pulses at a high frequency (around 4-6 GHz) to control our qubit. The two mixers we used are fabricated by *Marki Microwave Inc.* with the following specifications

Model	IQ-4509	M07078
RF [GHz]	4.5 to 9.0	4.0 to 8.0
LO [GHz]	4.5 to 9.0	4.0 to 8.0
IF [MHz]	DC-500	DC-500
Conversion Loss [dB]	5.5	7
Phase Deviation [deg]	4	3
Amplitude Deviation [dB]	0.3	0.3
LO-RF Isolation [dB]	30	22
LO-IF Isolation [dB]	20	20

Table 3.1: Specifications of the IQ-mixers.

The conversion loss is discussed in section 3.3. The phase deviation is a measure for the imbalance of the relative phase between the signals on the IF-ports, where the amplitude deviation is just the logarithm of the ratio between the squared amplitudes on the I and Q channel.

3.1 The ideal IQ-mixer

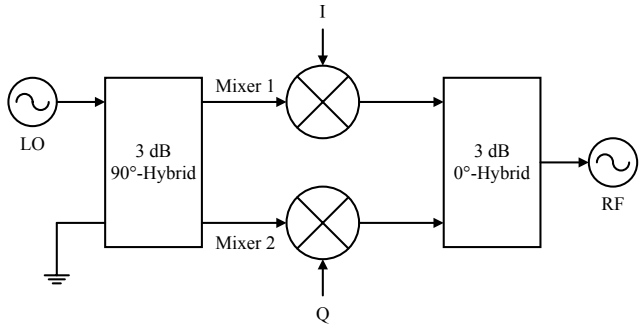

Figure 3.3: Block diagram of an IQ-mixer.

Figure 3.3 shows a block diagram of an IQ-mixer. The LO-signal (Local Oscillator) is split up in the 90 degree hybrid, which are then in phase quadrature. Each of the mixers multiplies then one of the split signal with one of the IF (I and Q) inputs which are then added in the Hybrid without any additional phase shift. So, the output signal at the RF-port can be calculated, by assuming three input signals

$$LO \quad : \qquad v_{LO}(t) = A_{LO} \cos(2\pi f_{LO} t) \tag{3.1}$$

$$I \quad : \qquad v_I(t) = A_I(t) \cos(2\pi f_I t) \tag{3.2}$$

$$Q \quad : \qquad v_Q(t) = A_Q(t) \cos(2\pi f_Q t - \phi) \tag{3.3}$$

The LO-signal with time independent amplitude A_{LO} is first split up into two 90 degree phase shifted signals

$$\xrightarrow{0^\circ} \quad \frac{A_{LO}}{\sqrt{2}} \cos(2\pi f_{LO} t) \tag{3.4}$$

$$v_{LO}(t) = A_{LO} \cos(2\pi f_{LO} t) \tag{3.5}$$

$$\xrightarrow{90^\circ} \quad \frac{A_{LO}}{\sqrt{2}} \sin(2\pi f_{LO} t) \tag{3.6}$$

The output of each mixer is given by the product of the LO and IF signals:

$$v_1(t) = v_I \cdot \frac{A_{LO}}{\sqrt{2}} \cos(2\pi f_{LO} t) \tag{3.7}$$

$$= \frac{A_{LO} A_I(t)}{\sqrt{8}} \{\cos(2\pi (f_{LO} + f_I) t) + \cos(2\pi (f_{LO} - f_I) t)\} \tag{3.8}$$

$$v_2(t) = v_Q \cdot \frac{A_{LO}}{\sqrt{2}} \sin(2\pi f_{LO} t) \tag{3.9}$$

$$= \frac{A_{LO} A_Q(t)}{\sqrt{8}} \{\sin(2\pi (f_{LO} + f_Q) t - \phi) + \sin(2\pi (f_{LO} - f_Q) t + \phi)\} \tag{3.10}$$

If the two IF signals are in phase quadrature, i.e. $\phi = \pi/2$ with the same frequency $f_I = f_Q \equiv f_{IF}$ and by assuming the same time dependent amplitude, i.e. $A_I(t) = A_Q(t)$ the *upper sideband* at frequency $f_{LO} + f_{IF}$ vanishes. In the second hybrid, the signals of the two mixers are combined without any phase shift

$$v_{RF}(t) = v_1(t) + v_2(t) = \frac{A_{LO}\, A_I(t)}{\sqrt{2}} \cos\left(2\pi \left(f_{LO} - f_{IF}\right) t\right) \tag{3.11}$$

We see that the IQ-mixer has then the effect of *up-converting* the IF signals to higher frequencies without changing its shapes, which means, that the amplitude of the IF-waveform is just multiplied by the constant factor $A_{LO}/\sqrt{2}$ but the phase is still the same. The sum and difference frequencies, $f_{LO} \pm f_{IF}$, are called the *sidebands* of the IQ-mixer. The spectra of the input and output signals are shown in the Figure 3.4. Notice that in the discussed case, only the signal with a frequency of $f_{LO} - f_{IF}$ should be visible at the output, where the upper sideband signal at $f_{LO} + f_{IF}$ should vanish. The input frequencies are located at f_{LO} and f_{IF}.

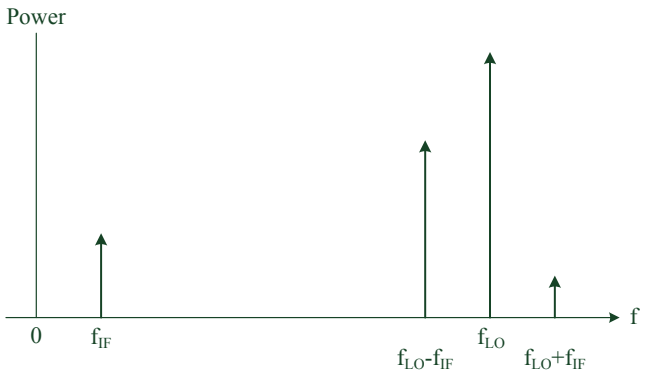

Figure 3.4: Spectra of the up-conversion process.

This behavior of an IQ-mixer is idealised as mentioned before, since there is no loss of signal and only one sideband should be visible in the considered case and this can only be achieved by assuming a perfect 90 degree phase shift in the first hybrid and by an identical mixing process of the two split signals in each mixer.

3.2 Nonlinearities

A mixer is a nonlinear element since there occurs additional frequencies at the output. Physically, the characteristic voltage-current curve of a Schottky diode can be modeled as a nonlinear resistor, see Figure 3.5, which causes the nonlinear behavior of a mixer.

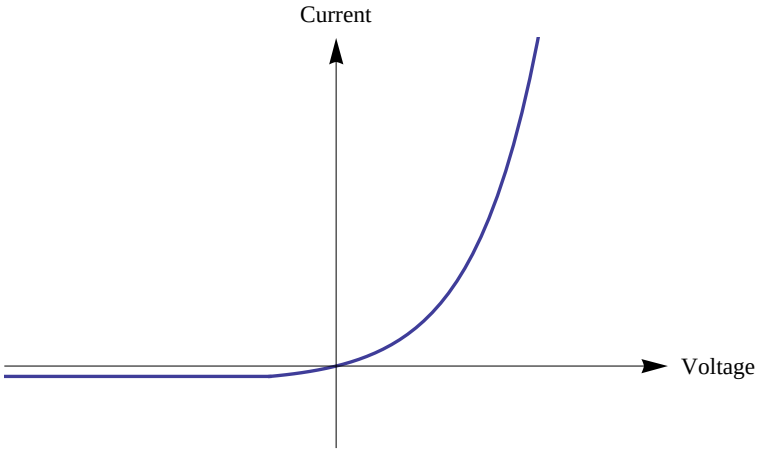

Figure 3.5: V-I characteristics of a Schottky diode.

Every nonlinear component can generate a wide variety of intermodulation disortions (IMD) and other products of the input frequencies [18]. In the discussed case in chapter 3.1 one would therefore see some additional peaks in the spectrum space which are located at multiples of the IF frequency around the sidebands. In the most general sense, the output response (v_o) of a nonlinear device can be modeled as a Taylor series in terms of the input signal voltage v_i

$$v_o = a_0 + a_1 v_i + a_2 v_i^2 + a_3 v_i^3 + ... \tag{3.12}$$

where the Taylor coefficients are defiened as

$$a_0 = v_0 [0] \tag{3.13}$$

$$a_1 = \frac{\partial v_o}{\partial v_i} [v_i = 0] \tag{3.14}$$

$$a_2 = \frac{\partial^2 v_o}{\partial v_i^2} [v_i = 0] \tag{3.15}$$

and higher order terms. If a_0 is the only nonzero coefficient in the Taylor series, the input signal (AC signal) will be converted into DC. If a_1 is the only nonzero

coefficient, one has a linear attenuator ($a_1 < 1$) or amplifier ($a_1 > 1$). And if a_2 is the only nonzero coefficient, one can achieve mixing signals. Usually, practical devices have more than one nonzero coefficient.
Now, consider a *two-tone* input voltage, with frequencies f_1 and f_2, i.e.

$$v_i = V_0 \left(\cos 2\pi f_1 t + \cos 2\pi f_2 t\right) \tag{3.16}$$

By using the above expansion 3.12, the output is given by

$$\begin{aligned} v_o = a_0 \quad &+ \quad a_1 V_0 \cos 2\pi f_1 t + a_1 V_0 \cos 2\pi f_2 t + \frac{1}{2} a_2 V_0^2 \left(1 + \cos 4\pi f_1 t\right) && (3.17) \\ &+ \quad \frac{1}{2} a_2 V_0^2 \left(1 + \cos 4\pi f_2 t\right) + a_2 V_0^2 \cos 2\pi \left(f_2 - f_1\right) t && (3.18) \\ &+ \quad a_2 V_0^2 \cos 2\pi \left(f_1 + f_2\right) t + \Theta\left(v_i^3\right) && (3.19) \end{aligned}$$

where $\Theta\left(v_i^3\right)$ is representative for third and higher orders. The output spectrum consists of harmonics which can be written in the form

$$m \cdot f_1 + n \cdot f_2 \tag{3.20}$$

with m,n=0,±1,±2,±3,.... These combinations of the two input frequencies are called *intermodulation products*, and the *order* of a given product is definied as $|m| + |n|$. Tabel 3.2 shows the frequencies of the intermodulation products up to the fourth order

first order	second order	third order	fourth order
f_1	$2f_1$	$3f_1$	$4f_1$
f_2	$2f_2$	$3f_2$	$4f_2$
	$f_2 \pm f_1$	$2f_2 \pm f_1$	$3f_2 \pm f_1$
		$f_2 \pm 2f_1$	$2f_2 \pm 2f_1$
			$f_2 \pm 3f_1$

Table 3.2: Output frequencies of first to fourth order two-tone intermodulation products, assuming $f_1 << f_2$.

If f_1 and f_2 are far apart, e.g. f_1=100 MHz, f_2=4.0 GHz, all the entries in table 3.2 with higher harmonics of f_2 can easily filtered out. The only signals which are located near f_2, are given by $f_2 \pm m \cdot f_1$, $m > 1$, and can't therefore easily filtered out. Notice that this additional signals are symmetrically distributed around the dominant frequency. Physically, the rectification of the LO signal to a DC power done in the diodes causes the intermodulations. So, the general treatment of the nonlinearities above just shows the so called *small-signal approximation* of the diode, where the voltage applied on a diode consists of a DC bias voltage and a small-signal

high frequency voltage. One can then expand the current in a Taylor series in terms of the total voltage applied on the diode around the DC bias voltage. However, in an IQ-mixer 2 mixers are used, where in every single mixer the LO and an IF signal is mixed. It is not possible to identify which of the two double balanced mixers cause which IMD, by just measuring the output spectrum. So, the frequency distribution of the nonlinearities of the IQ-mixer do not have to be symmetrically.

Figure 3.6 clearly shows the measured IMD's for the Mixer IQ-4509. The power

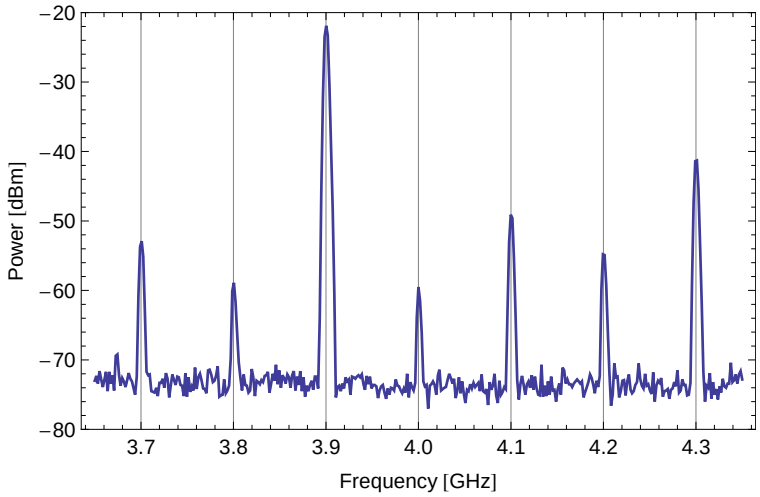

Figure 3.6: IMD's due to a high input amplitude (500 mV) at the I/Q ports. LO: 4.0 GHz, IF: 100 MHz and left Sideband at 3.9 GHz.

of nonlinearities are very large which could be achieved by applying a sinusoidal waveform on the I and Q port with a high amplitude of 500 mV. The drive level of the LO was at +16dBm and therefore in its linear regime, which is at the upper limit of the suggested LO powers (13 to 16 dBm). In this regime, the output voltage of the diodes is linear in the input power of the LO signal. The peaks at the frequencies 3.8 GHz and 4.2 GHz are caused by the second order intermodulations, where the additional signals at 3.7 GHz and 4.3 GHz can be ascribed to the third order nonlinearity of each single mixer. A detailed analysis of the additional peaks is discussed in a later section.

3.3 Mixer losses

The so-called *conversion loss* summarizes the 3 possible losses in a mixer:

1. mismatch loss
2. parasitic loss
3. junction loss

An important figure of merit is therefore the conversion loss of a mixer, which is defined as the ratio of available IF input power to the available RF output power, expressed in dB [18]:

$$L_C = 10 \log \frac{\text{available IF input power}}{\text{available RF output power}} \geq 0\,dB \tag{3.21}$$

Mismatch losses is a function of the impedance match at the RF and IF ports and occurs if the mixer port impedance and the source impedance are not matched. The mismatch loss is the sum of RF and IF port mismatch losses. This is one of the principal reasons for losses in mixers.[4]
In reality it's not possible to block all the unwanted leakages (parasitic loss), but for the up-conversion mixing it's only the original LO-signal which may disturb the spectrum since it is only frequency shifted by the much smaller IF from the sidebands. As shown later the LO leakage can be stashed away by applying a DC-offset to the I and Q ports. If only one sideband is desired at the output it is necessary that the signal on the I and Q channel are in phase quadrature with the same time dependent envelope where the modulating signals must have the same frequency.
Junction losses add noise to the input signals, which will then be diminished. This kind of loss is a function of the diode's V-I-curve and is therefore mainly generated in the mixers. For more details, see reference [4].

3.4 Calibration of the IQ-mixer

All different losses generate imbalances in the mixing process which can be divided into three categories:

DC-offsets: They are mainly caused by the 2 double balanced mixers and is a measure of the unbalance of the IQ-mixer. For an ideal mixer, the DC-offset is zero. DC-offset defines the IF output voltage when the IQ-mixer is used as a down-converter and only a LO-signal is applied where the RF-port is terminated in 50 ohms.[16]

Amplitude imbalance: An ideal IQ-mixer handles the I and the Q signal identically but one observes a slightly different amplification/attenuation on both channels, due to unbalances in both hybrids and different conversion losses in the two mixers.

Phase imbalance: These errors are caused by phase unbalances in the 90 degree hybrid and also occurs by different electrical length.

Taking all this errors into account leads to a correction of the input signals on the I and Q ports

$$I^* \quad : \qquad v_I^*(t) = (B(t) + e_3)\ K\ \cos(2\pi f_I\, t) \tag{3.22}$$

$$Q^* \quad : \qquad v_Q^*(t) = (C(t) \pm e_1)\ K\, e_2\ \cos(2\pi f_Q\, t - (\phi + \Delta\phi)) \tag{3.23}$$

where e_1 and e_3 are DC-constants, e_2 consider the amplitude imbalance and $\Delta\phi$ takes into account the phase imbalance. The 3 additional parameters allow to calibrate the IQ-mixer such that the output at the RF can be describe by equation (3.11).
By ignoring the discussed imbalances and just applying 90 degrees (i.e. $\Delta\phi = 0$) phase shifted sinusoidal waves on the I and Q channels with identical amplitude ($e_2 = 1$) and abstracting away from the DC-offsets ($e_1 = e_3 = 0$) the spectrum shows 3 peaks. Due to the phase- and amplitude imbalances, it's the main aim to determine $\Delta\phi$ and

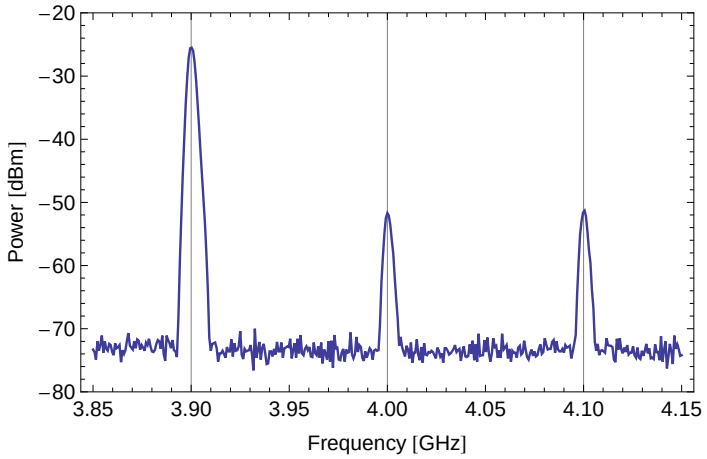

Figure 3.7: Uncalibrated IQ-mixer with the two sidebans and the LO leakage. LO: 4.0 GHz, IF: 100 MHz and left Sideband at 3.9 GHz. Notice that the power of the signals at 4.0 GHz and 4.1 GHz are not the same although it seems so in this plot. The IMD's are out of range.

e_2 which then minimize the right sideband at $f_{LO} + f_{IF}$, Fig. 3.8 a). But leakage of the LO signal is still visible and can be eliminated by the DC-offsets on the I/Q ports. This will vanish the signal at the LO-frequency which is exactly located between the two sidebands. A calibrated IQ-mixer should therefore only demonstrate one peak

on the spectrum analyzer, as shown in Figure 3.8 b). The amplitude and quadrature phase deviation of any IQ-mixer necessitate a calibration of the mixer at a certain LO and IF frequency/amplitude.

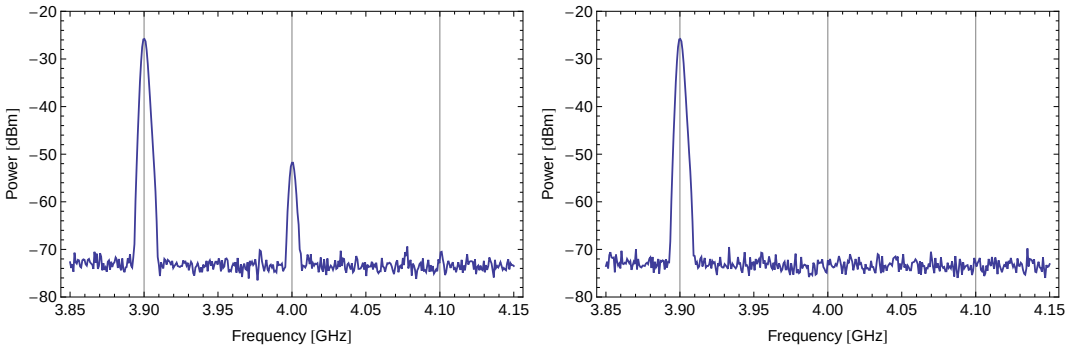

(a) (b)

Figure 3.8: a) After the phase and amplitude calibration ($e_2 = 1.053 \pm 0.001$, $\Delta\phi = (-5.7 \pm 0.1)$ deg). b) Final calibration, including applied DC-offsets ($e_1 = (3.3 \pm 0.1)$ mV, $e_3 = (-17.6 \pm 0.1)$ mV). The IMD's are out of range but still existing.

3.5 Automation of the calibration

As the calibration coefficients are frequency dependent it is useful to automate the calibration routine. This was realized by a *Labview-Program* which do this phase and amplitude calibration automated.
By fixing a sinusoidal signal on I with a certain amplitude, one varies the amplitude and phase of the sinusoidal waveform on the Q channel by simultaneously measuring the power of the upper sideband, which can be done with a spectrum analyzer (*Agilent E4407B*). One starts with the same Q-amplitude as on the Q channel and sweeps the relative phase around 90 degrees until a minimum power on the upper sideband has been found. In a next step, this minimum-phase is fixed and the Q-amplitude is swept until again a minimum in power has been found. This algorithm stops if three times after another the same minimum phase and amplitude was detected on the Q channel. Figure 3.9 demonstrates this algorithm visually.

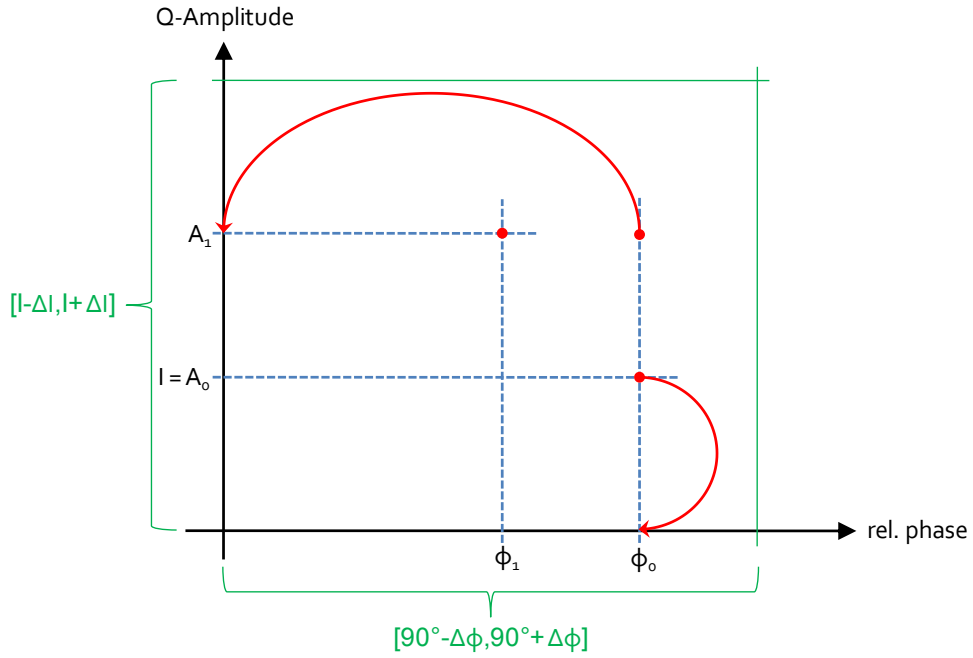

Figure 3.9: Algorithm of the Labview-program to find the minimum phase and amplitude at a fixed waveform on the I channel.

The waveforms in the usual experiments were generated by *Mathematica* as pattern files which were then uploaded onto an arbitrary waveform generator (AWG) and the waveform is output using a digital to analog converter (DAC). This is an intricate way for the mixer calibration as a lot of different sinusoidal waveforms are needed, depending on the accuracy. A *SubVI* now generates the sinusoidal waves with modifiable amplitude and phase, which save time and computer memory given that only the currently required waveforms are directly generated and sent to the AWG.

Figure 3.10 shows a typical plot, where only one strong minimum is visible if a large range of amplitudes and relative phases on the Q channel is scanned.

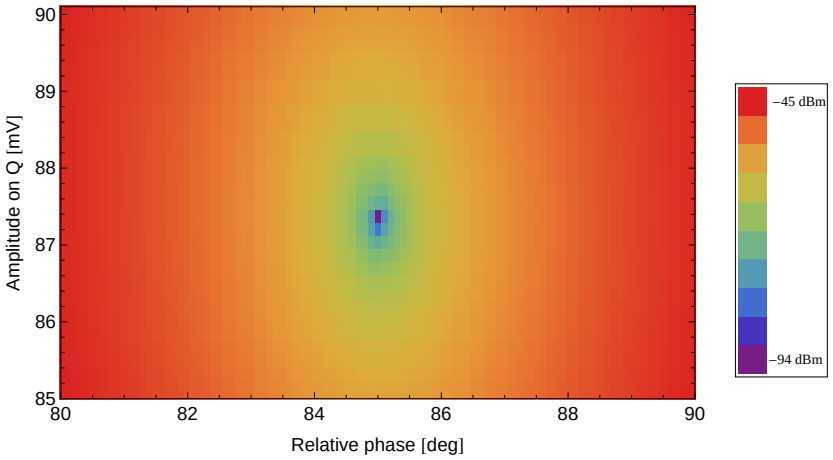

Figure 3.10: Typical calibration plot, where blue represent a low power at the right sideband (3.1 GHz) and red a high one. LO: 3.0 GHz, IF: 100 MHz

A LO-frequency of 3.0 GHz was chosen with a power of +16 dBm and the I-channel settings are the following: amplitude = 85 mV, IF = 100 MHz. This yields a strong minimum for the Q-channel: phase = $(85.0 \pm 0.1)^\circ$ and amplitude = (87.38 ± 0.17) mV. The phase imbalance is therefore $\Delta\phi = (5.0 \pm 0.1)^\circ$ and the amplitude imbalance $e_2 = 1.028$.

The next two plots shows a cross-section through the minimum point in both direction, where the power is now given in a linear scale. Notice the smaller resolution in amplitude compared to the phase-resolution. Anyway, the phase and amplitude are sensitive at the minimum point.

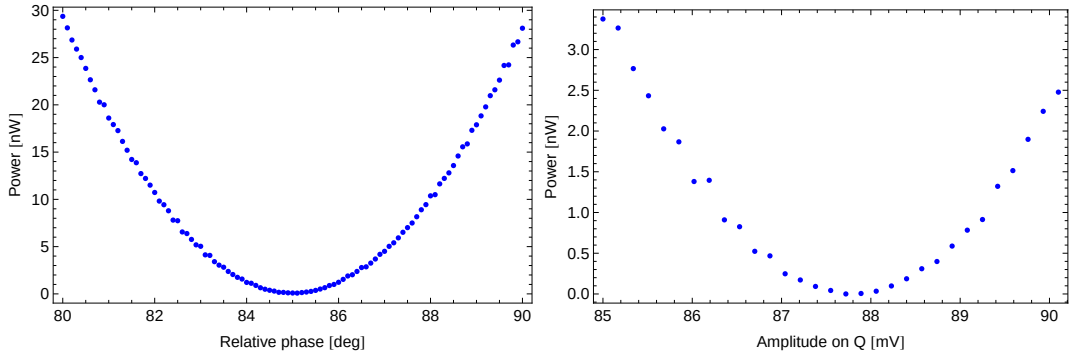

(a) (b)

Figure 3.11: (a) Cross-section in the phase direction. (b) Cross-section in the amplitude direction.

This calibration can be repeated for different amplitudes on one channel (here: I) by implementing a loop in the LabView-VI. To get a significant statistic, this has be done for 187 different amplitudes up to 400 mV. The IF is again 100 MHz and the LO is chosen to be at 4 GHz with +16 dBm power. By sweeping now the amplitude of channel I and detecting the calibrated amplitude of the other IF-input amplitude yields a linear relationship, Figure 3.12 left. Notice that the phase imbalance is already corrected.

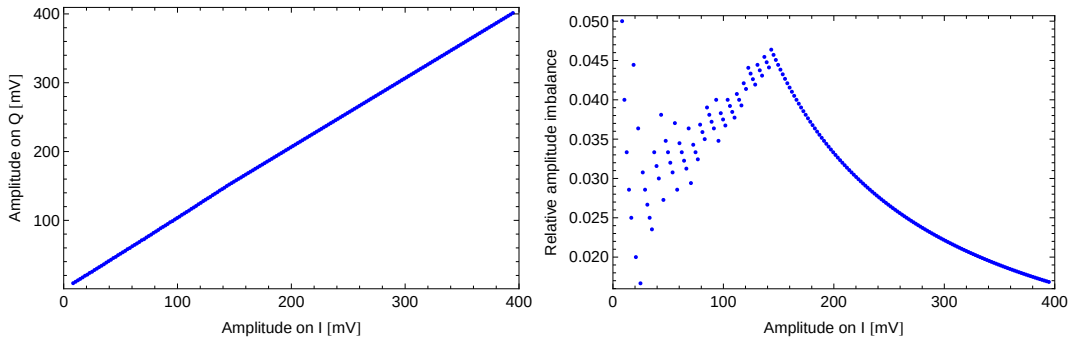

Figure 3.12: a) Calibration data of the amplitudes yields a linear relation.

The relative amplitude imbalance is defined as $(V_Q - V_I)/V_I$, and should be near 0. For low amplitudes up to 150 mV on the I port, the imbalance increases, but decreases for larger amplitudes than 150 mV, see Figure 3.12 right. The deviation from point to point for low amplitudes is also bigger than for I-amplitudes > 150 mV.

There is no obvious dependence between the amplitude of I versus the calibrated phase which says that $\Delta\phi$ is largely independent of the I-amplitude. The different relative phases are distributed in a small range (between 84.1° and 85.0°)

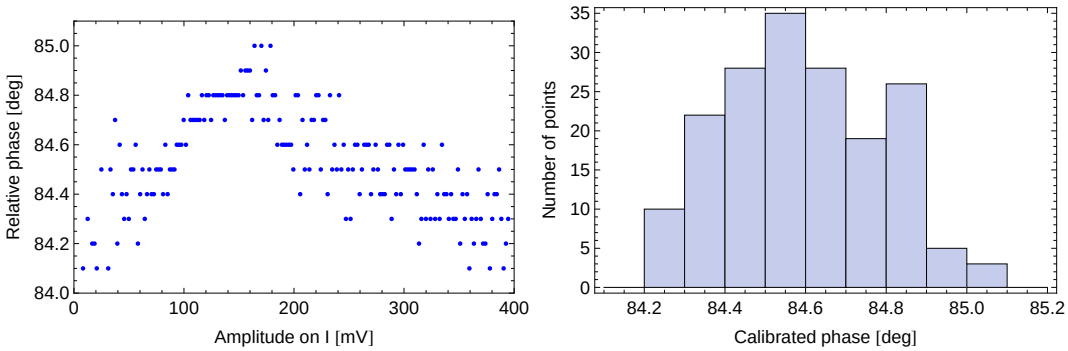

(a) (b)

Figure 3.13: (a) Amplitude sweep versus the calibrated phase at which the right sideband (4.1 GHz) power is indistinguishable from the noise level. (b) Corresponding histogram.

The discrete distribution along the vertical axis has to do with the accuracy of the phase which is ±0.1°. This choice has to do with the sampling rate of the AWG: 1 GS/s, and the relative phase between the two channels were changed around 90 deg by ±5°, so there are 100 digital points per period for a 100 MHz sinusoidal signal and therefore a resolution of $10°/100 = 0.1°$ was chosen. The question is now, if it is possible to fix a relative phase for a large range of I-Amplitudes and to use a linear relation between the I- and Q-Amplitudes, since the the calibration has a sensitive minimum, see Figure 3.12. To show this, the mixer was phase-calibrated at a fixed I and Q amplitude of $V_{pp} = 500\,mV$ (V_{pp} means the peak-to-peak voltage of the sinusoidal waveform, i.e. 2 times the amplitude), with the calibration parameters: $\phi + \Delta\phi = 90° - 9.2°$, DC-offset of Q: (-2.2 ± 0.1) mV and of
I: (5.5 ± 0.1) mV. The amplitude imbalance is given by e_2=500/482. The LO signal has a frequency of 5.0 GHz and a power of 16 dBm, where the M07078-mixer was used.
To analyse the behavior of a fixed calibrated phase for different IF-amplitudes, one has to define the *Rejection ratios*

Carrier Rejection: The amount of carrier (=LO-signal) measured in dB below the desired output signal when a coherent signal of equal amplitude and 90° phase difference is applied to the I and Q ports. This definition can be used for the calibrated and also for the uncalibrated case.

Sideband Rejection: The amount of undesired sideband measured in dB below the desired sideband under the same conditions as the carrier rejection measurement [15].

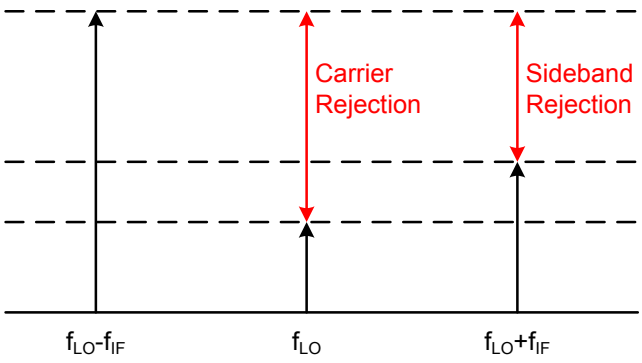

Figure 3.14: Definition of the different rejections.

Figure 3.15 a) presents the measured rejection ratios. The point of calibration was chosen arbitrary to be at $V_{pp} = 500$ mV, because the maximum output voltage of the AWG is 1 Volt. It's to be expected that the largest rejection is to be found at the calibration point, i.e. $V_{pp} = 500mV$, but this isn't true for the carrier rejection. This can be explained by the accuracy of the DC-offsets which were in this case ± 0.1 mV, since another DC supply was used for this experiment.
For amplitudes larger than the calibration point, the carrier rejection remain still at a high level ($\geq 40dB$) where the sideband rejection is quite sensitive of increasing amplitudes.

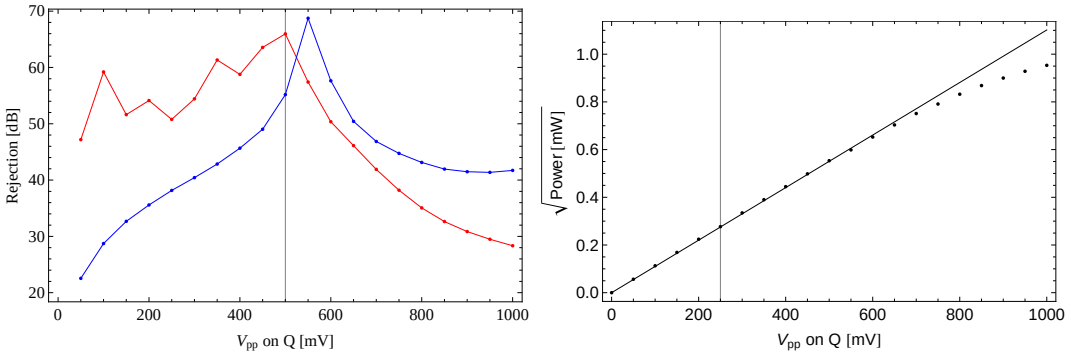

(a) (b)

Figure 3.15: (a) Blue: Carrier Rejection, Red: Sideband Rejection. (b) Left sideband amplitude versus the Input amplitude on the IF signals. The line shows a linear interpolation of the first 13 points. For large amplitudes a deviation from the linear correlation is visible.

For this large amplitude range it's also meaningful to take the IMD's into account. The rejection for the IMD's is again the relation between the wanted signal at 3.9 GHz and the nonlinearities which are multiplies of 100 MHz apart (Figure 3.16).

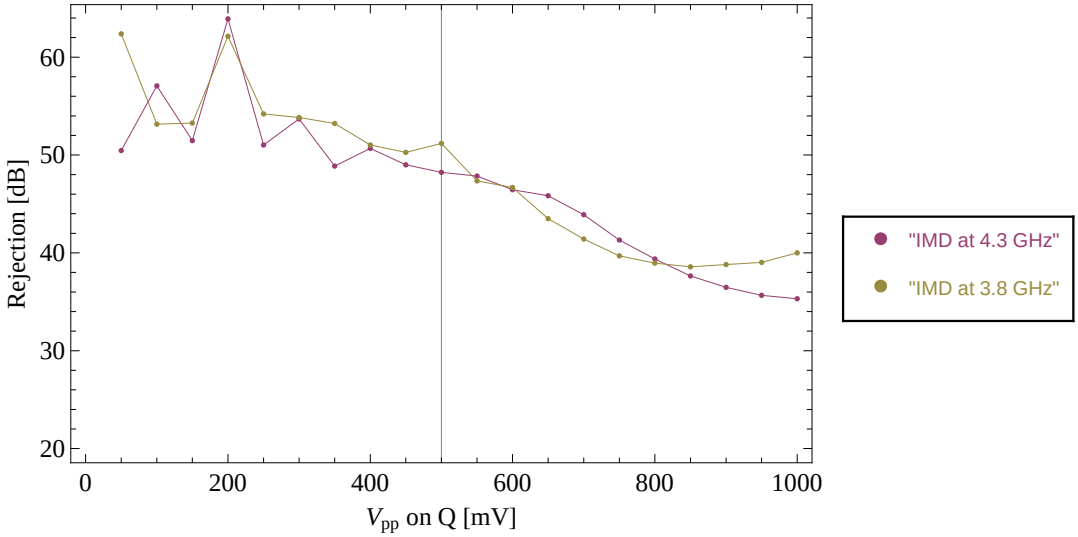

Figure 3.16: Rejection of the nonlinearities in the calibrated case.

Is's obvious that the rejection ratios of the two intermodulation distortions get smaller for increasing amplitudes of the IF signals. But even for large amplitudes, the sideband rejection (Figure 3.15 a)) is much smaller than the rejection of the IMD and would therefore have a bigger influence on the desired output.

3.6 Calibrated versus uncalibrated IQ-mixer

In this section the measurements are done with the M07078. It's interesting to see the difference between the calibrated and the uncalibrated case of the IQ-mixer. Firstly, measuring the sideband rejection for the two cases shows the big difference between them. The LO frequency was set at 4.0 GHz with +16 dBm power, then a sinusoidal waveform was applied at the I and Q ports, where the amplitude and phase calibration was arranged for every point to obtain the maximum signal on the lower sideband at 3.9 GHz. The DC-offset were set at a Q-Amplitude of 200 mV and never changed again for other amplitudes: Q-Offset = (20.1 ± 0.2) mV and I-Offset = (37.7 ± 0.2) mV.Figure 3.17a) shows the measured sideband rejection for the calibrated and the uncalibrated mixer.

The building up effect of the red curve in Figure 3.17 a) for small input amplitudes (<200 mV) can be explained by the small power of the lower sideband peak at this voltage of the I and Q channel. But for higher amplitudes the difference is enormous

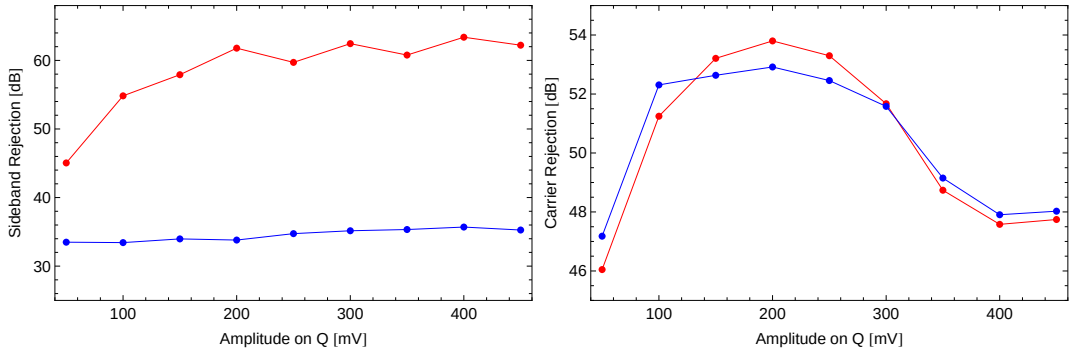

(a) (b)

Figure 3.17: a) Sideband rejection of the calibrated (red) and uncalibrated (blue) IQ-mixer. b) Carrier Rejection

(about 25 dB) between the two curves. This big difference can't be observe for the carrier rejection, where the two lines are almost the same and vary in a small range of around 8 dB, but there is no obvious dependence of the carrier rejection on the amplitude.

As mentioned the calibration has be done for every change of the IF-amplitudes. Once again a linear relation between the amplitudes on the I and Q is observable, Figure 3.18 a), but the phase-calibration does not look the same for small amplitudes (<150 mV) as the other IQ-mixer, Figure 3.18 b) and 3.13 a). Notice that for larger amplitudes the relative phase still decrease.

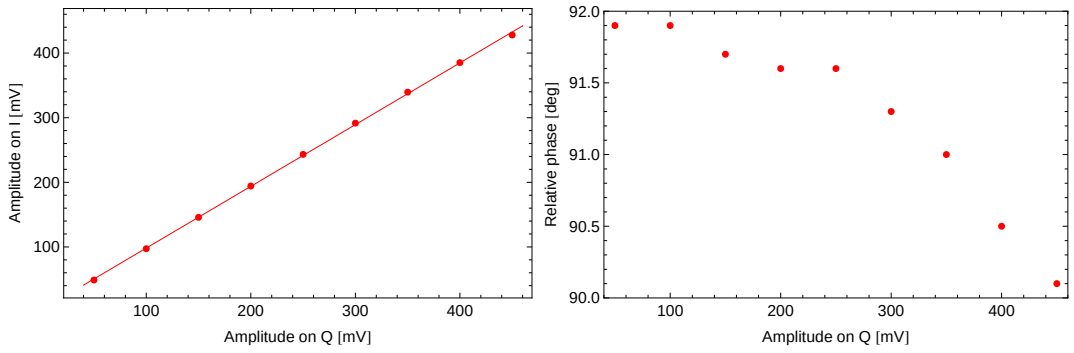

(a) (b)

Figure 3.18: a) Amplitude-calibration, solid line shows a linear interpolation. b) Phase-calibration, no obvious dependence on the amplitude.

To do sideband transitions on the qubit, high drive amplitudes are required, since the $|g,0\rangle \rightarrow |e,1\rangle$ transition can only be driven with two photons, as discussed in the section about the *sideband transitions*. So the pulses generated with the IQ-mixer need a high power, although they will be amplified after the generation. Anyway, it is useful to see an application of the calibration process. Mostly, Square- and Gaussian pulses are needed for the experiments which is the reason to apply the calibration on these shapes. These pulses were generated in a SubVI of Labview by multiplying the required envelope with a sinusoidal waveform of a given IF-frequency. The generated table was then directly sent via LAN to the arbitrary waveform generator (AWG) *Agilent N8242A* , with 1.25 GS/s and 10 Bit resolution. For the uncalibrated case, these two pulses have the same envelope ($A_I(t) = A_Q(t)$) but the carrier wave are 90° phase shifted without considering the phase ($\Delta\phi$) and amplitude imbalances (e_2), but with the same IF-frequency. One will therefore also see the LO-leakage and the upper sideband signal in the frequency space. It's therefore necessary to determine the imbalances of the phase and the amplitude. To do a calibrated pulse, one just applies the single sinusoidal (time independent envelope) waves on each IF-port and does the calibration on them, which then yields the phase and amplitude correction terms. The calibration also includes the additional DC-offsets on the IF-ports to get rid of the leakage (LO-signal). These carrier waves can then be multiplied with the desired envelope. The pulses were then led to the I and Q port of the mixer via two SMA-cables. An Analog Signal Generator (*Agilent E8257D*) provide the LO-signal (6.0 GHz at +16 dBm power).

To record enough points, a 100 ns long Gaussian pulse was chosen, for a sampling rate of 1.2 GS/s, we get therefore a pulse form built by 120 points. The left Figure below shows the uncalibrated (blue) and the calibrated (red) version of the pulse shape, where the red line is vertically shifted around -50 mV for better comparison. At a this large scale they almost look the same, but by zooming-in, a 200 MHz oscillation is visible at the uncalibrated measurement, which is caused by the upper sideband since the two sidebands are 200 MHz apart from each other.

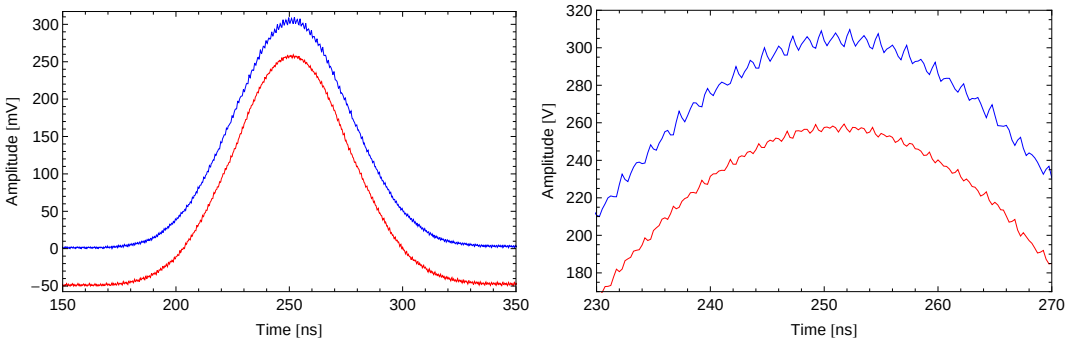

(a) (b)

Figure 3.19: a) 100 ns Gaussian pulses, blue: uncalibrated, red: calibrated with a -50 mV offset for better visibility. b) 200 MHz oscillations on the uncalibrated pulse.

An other important pulse is the square one. A similar result can be observed, but there is also an oscillation at the beginning at the end of the pulse, see Figure 3.21, which can be explained by the finite spectrum of the AWG to generate the pulse, since it can't use an infinity range of frequencies. Figure shows qualitatively the effect of a finite frequency range. Mathematically, a finite range was taken into account for the inverse Fourier transformation of a sinc-function, since the sinc-function is the Fourier transform of a square pulse. And the asymmetric behavior of this additional

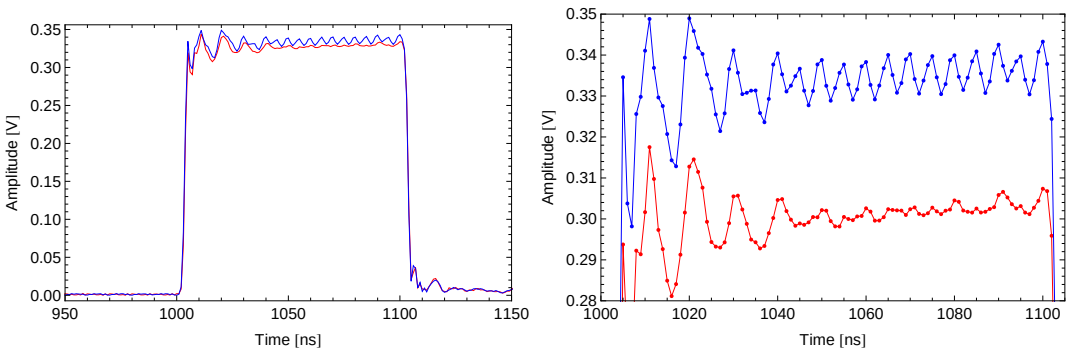

(a) (b)

Figure 3.20: a) 100 ns Square pulses, blue: uncalibrated, red: calibrated. b) 200 MHz and 100 MHz oscillations on the uncalibrated pulse.

oscillation which only occurs at the beginning and at the end of the pulse can be explained by a low-pass filter, due to the SMA cables which acts as a low-pass filter. Figure 3.21 b) shows qualitatively the effect of a SMA cable on a square pulse, which can therefore explain the asymmetric pulse shape of the measured square pulse.

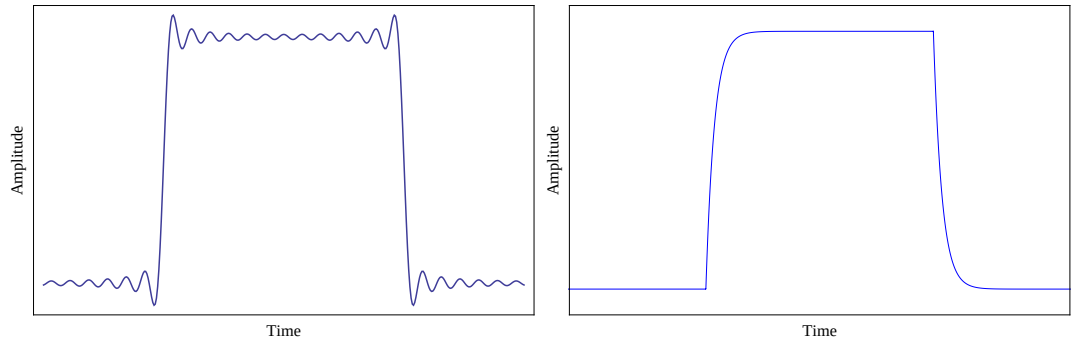

Figure 3.21: The effect of a finite frequency range in the inverse Fourier transformation of a sinh-function.

3.7 One-Qubit Tomography

Figure 3.22 shows a schematic representation of the experimental setup. A sample with two qubits installed inside a dilution refrigerator at a temperature of around 15 mK, with microwaves for control and readout generated at room temperature was used for experiments. In my experiment only Transmon A was use, where the other one was tuned to a small transition ($|g_B\rangle \rightarrow |e_B\rangle$) frequency, such that the two Transmons won't interfere each other. The pulses are generated with an arbitrary waveform generator with 1 ns resolution which is connected to the IF-ports of the IQ-mixer and then upconverted to the desired transition frequency. The RF signals are filtered and attenuated several times to minimize thermal noise. The DC signals are low-pass filtered with stainless steel powder filters at different temperature stages [23]. The magnetic flux, which tunes the qubits is generated by two different coils. One of the coils has an inner diameter of 4 mm and couples in good approximation to only one qubit, where the other coil has a diameter of 16 mm and couples to both qubits. Adjusting the current of both coils gives the possibility to tune the flux through the two qubits individually. Operations on the qubits are done by using charge gate lines. The gate line is a wave guide, which is capacitively coupled to the reservoir of one of the qubit which gives the opportunity to manipulate the qubit individually. Each gate line is then connected to a microwave generator. Between the generator and the gate line a mixer is implemented. The mixer is used to modulate the amplitude and the phase of the microwave pulse [14].

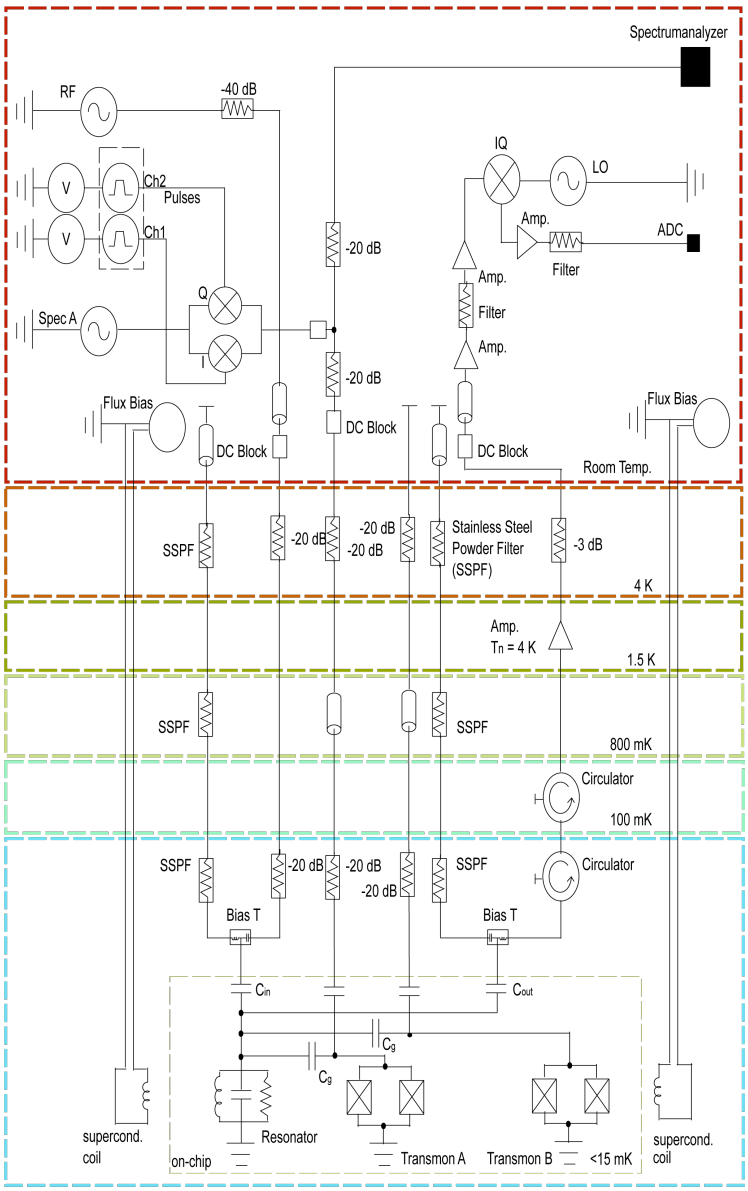

Figure 3.22: The graphic shows schematically the measurement and control circuitry. The signal generation for measurement and control pulses are pictured in the top left corner and the readout and calibration output are placed in the top right corner. The different temperature stages are indicated by color. The graphic shows all filters, attenuators and amplifiers. The two coils which have been used for individual detuning of the qubits are depicted on the side of the image.[14]

The pulse sequence of the one-qubit tomography is shown in Figure 3.23, where first a 15 ns preparation pulse is applied to initialize the qubit state and after 5 ns one applies the tomography pulses which are square pulses on the I and Q channel with different amplitudes. To readout the qubit state, a pulsed measurement was done at the end of the sequence. The advantage of pulsed measurement compared to the continuous one, which means that the resonator has always been populated with photons (at the resonator frequency) during the whole sequence, is that no AC-Stark shift occurs. On the other hand, continuous measurement has the clear advantage that one can observe the qubit before, while and right after applying the operation pulses.

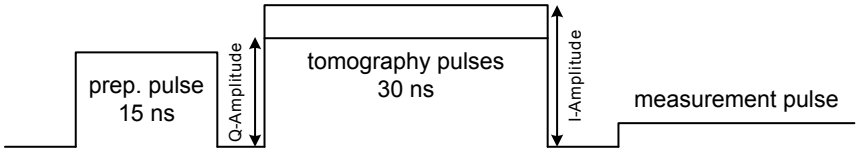

Figure 3.23: The pulse sequence starts with a preparation pulse of 15 ns length followed by the tomography pulses with different amplitudes and at the end a measurement pulse to determine the population of the excited state of the qubit

By plotting the population of the excited state in a 2 dimensional graphic in which the Q- and I-amplitudes were changed independently on each axis one got the 2 dimensional tomography of the qubit. It no preparation pulse is applied, the initial state of the qubit is the ground state, a π_x-pulse initialize the qubit into the excited state. To reach the superposition states one just applies a $\pi/2_{x,y}$-pulse, the rotation around the x-axis yields the $|0\rangle + i|1\rangle$ state, where the rotation around the y-axis prepares the qubit in the $|0\rangle + |1\rangle$ state. Figures 3.24 till 3.26 show the results of this 4 measurements and compare it with its corresponding simulation which was just done by calculating the population of the excited state if one performs a manipulation described by $H = \hbar\Omega_x\sigma_x + \hbar\Omega_y\sigma_y$. The power of the RF generator has been set to a value of -20 dBm at a frequency of 6.45 GHz. The measurement have been averaged 655350 times. The transition frequency for the qubit was set to 4.6 GHz, which corresponds to a detuning of 1.85 GHz. The pulse length was chosen to be 30 ns. One can clearly see the concentric circles which is an indication that a full phase and amplitude control is possible on the IQ-mixer, since the amplitude and phase are independent of each other, otherwise one would see ellipses.

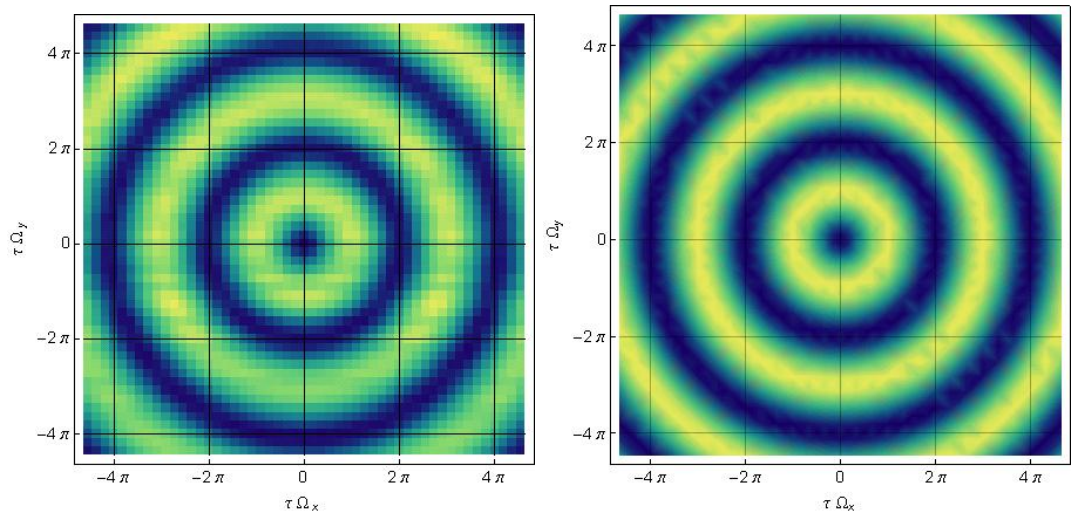

Figure 3.24: Initial state: ground state. The graphics show the population of the excited state, where yellow is 1 and blue is 0. The right hand side is a simulation and the left hand side is the measurement.

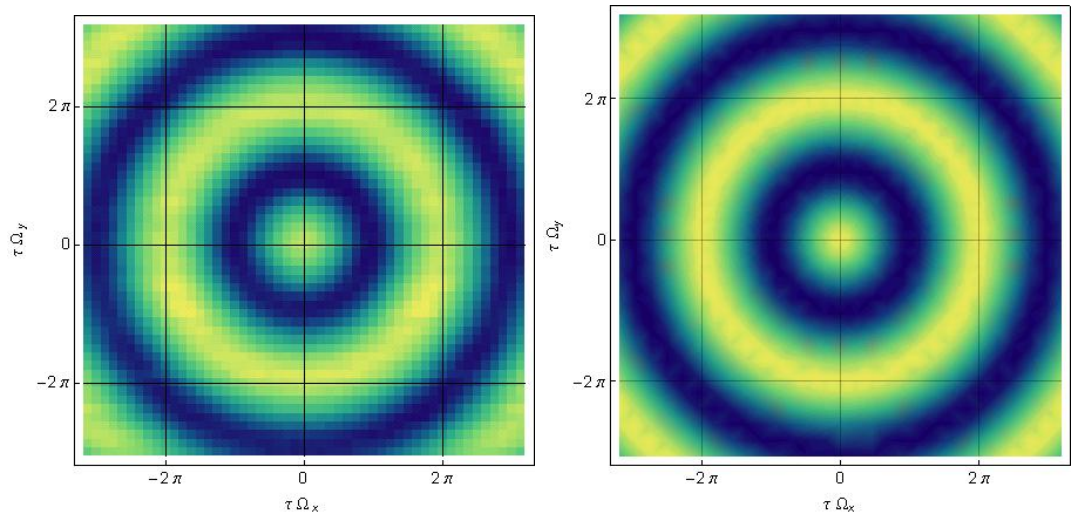

Figure 3.25: Initial state: excited state. The graphics show the population of the excited state, where yellow is 1 and blue is 0. The right hand side is a simulation and the left hand side is the measurement.

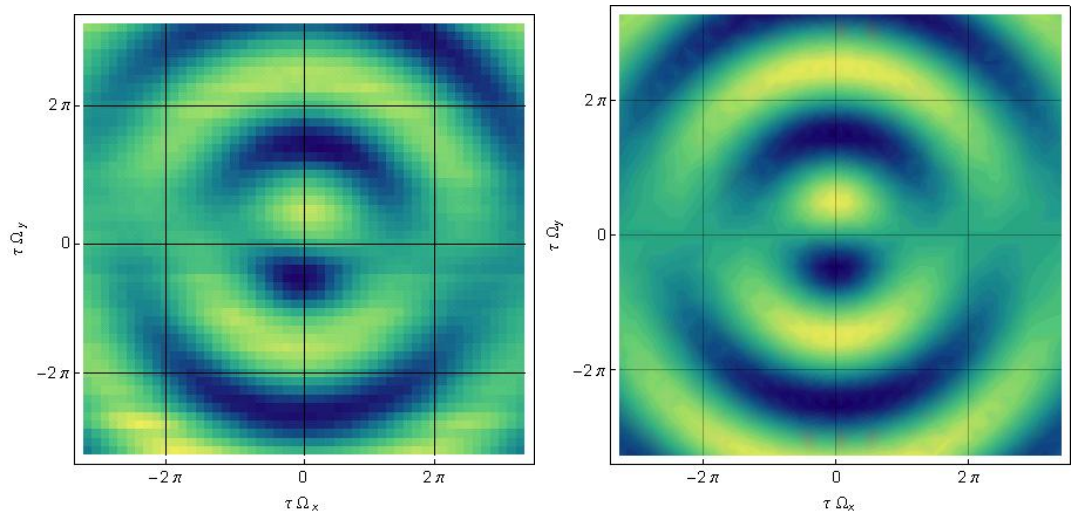

Figure 3.26: Initial state: superposition state $|0\rangle + |1\rangle$. The graphics show the population of the excited state, where yellow is 1 and blue is 0. The right hand side is a simulation and the left hand side is the measurement.

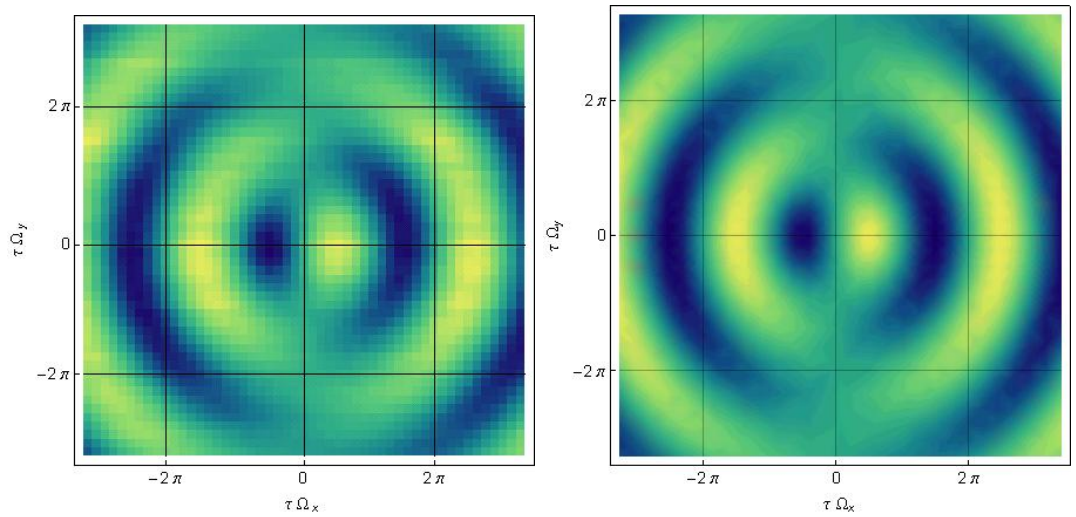

Figure 3.27: Initial state: superposition state $|0\rangle + i|1\rangle$. The graphics show the population of the excited state, where yellow is 1 and blue is 0. The right hand side is a simulation and the right hand side is the measurement.

4 Sideband transitions

The new setup used to drive the qubit sideband transition, which needs a high power signal, is shown in Fig.4.1. The upper IQ-mixer can be used for direct qubit transitions, where the 3 dB attenuator prevents reflections between the mixer and the splitter. On the lower setup, an additional amplifier with a gain of ≈30 dB has been installed to reach the desired output power for qubit sideband transitions. A splitter at the output allows to install the spectrum analyzer to calibrate the IQ-mixers.

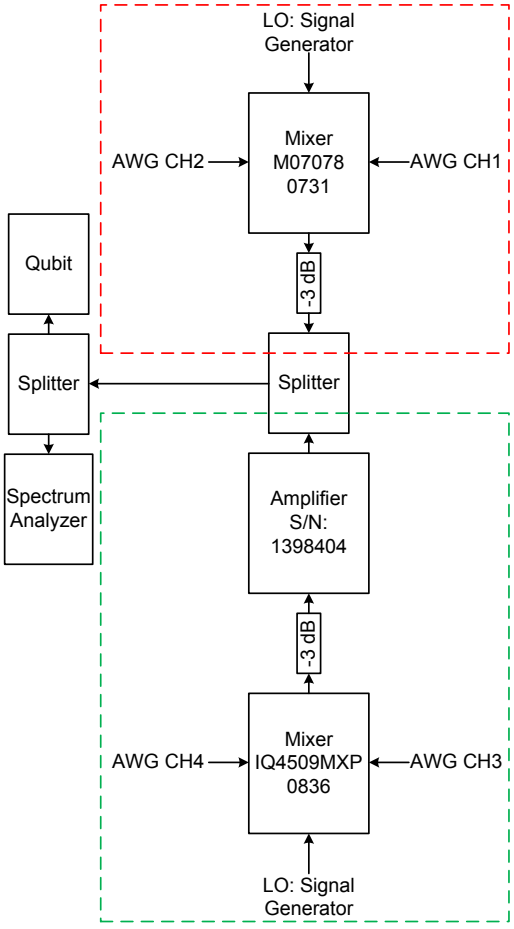

Figure 4.1: Final Setup for sideband transition (green dashed box) and single qubit drive (red dashed box). Channel 1/3 are connected to the I-port of the mixer, and channel 2/4 to the Q-port. The additional attenuators of 3 dB should avoid reflections.

The amplifiers are manufactured by *MITEQ N.Y.*and have a gain between 28 dB and 31 dB, depending on the frequency. The test result of the *AFS3-00101200-40-20P-4*(SN: 1398404) is presented here. A power supply was applied to the amplifier with a DC-voltage of +15 V (current: 263 mA) and the frequency range of the incoming signal is given by (100-12000) MHz. An important Figure Of Merit (FOM) is the 1 dB compression point which defines the output level at which the amplifier's gain is 1 dB less than the small signal gain (linear behavior), or is compressed by 1 dB. For the tested device this point is reached when the output power is +20 dBm (datasheet). It's quite important to heat up the amplifier ($\approx$ 10 minutes), since the amplification is about 2 dB larger in the cold case, but when the amplifier has reached its working temperature the gain is not time dependent anymore. The gain over the whole frequency range was measured, see Fig. 4.2. Up to 11 GHz the amplifier works in its

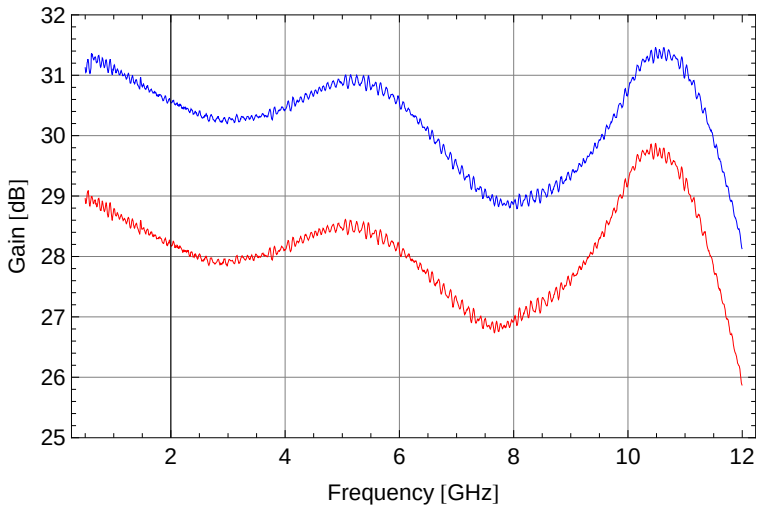

Figure 4.2: Gain depending on the frequency. Blue: Cold case, Red: Warmed up by bias.

predicted gain range, but above this frequncy the gain is around 1 dB smaller. Since we later need a range of 3-6 GHz it doesn't matter. To check the linear regime of the amplifier one has to measure the output power for different input powers. Near the 20 dBm output the nonlinear behavior should be visible.

The input signal has a frequency of 3.0 GHz. Extracted from the previous measurement the gain is 27.9 dB at this frequency. A linear fit up to an input power of -21 dBm is plotted (solid green line), which clearly indicates the nonlinearity of the amplifier near 20 dBm (output). The compression point can therefore be extracted depending on the input power: (-6.5±0.5) dBm input power. For the used frequency of 3.0 GHz, the output power is (21.4±0.5) dBm.

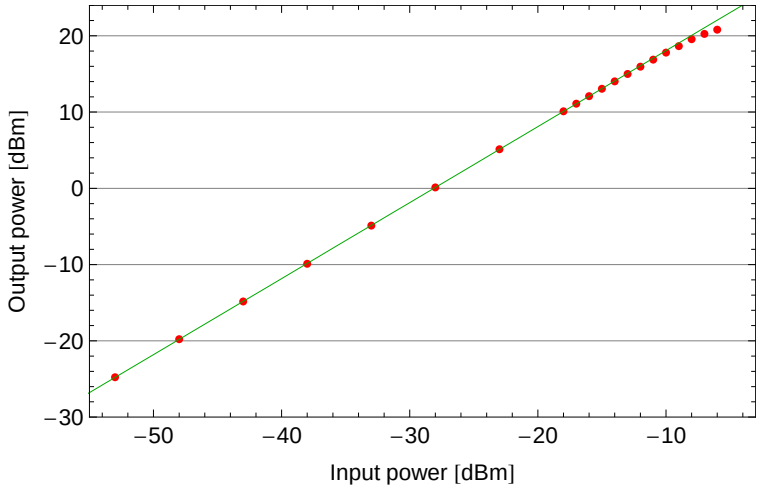

Figure 4.3: Output versus Input power. Solid line is a linear interpolation of the low power regime.

An other important fact is that a +20 dBm output power has been reached with this amplifier. The next figure illustrates a more accurate way to find the compression point using the same data. Here, the gain is plotted versus the input power. If the low-power gain is compressed by 1 dB one has found the compression point.

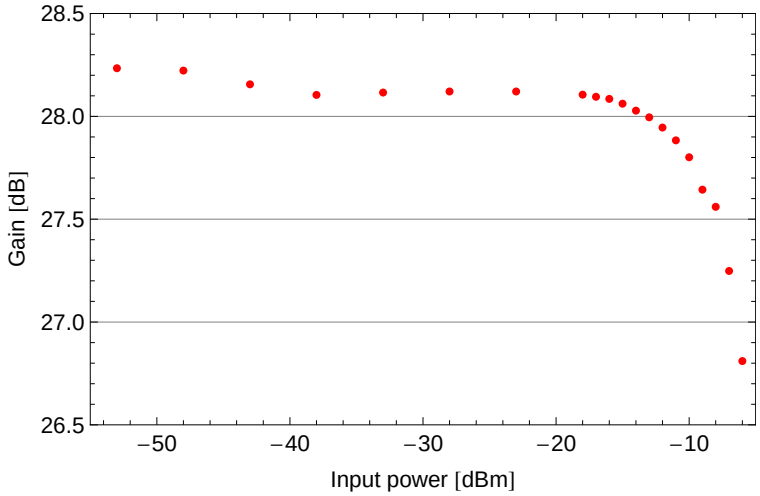

Figure 4.4: More accurate way to find the compression point.

To show the operability of the new setup, the qubit sideband Rabi oscillations has

been measured. The bare fundamental resonant frequency of the coplanar waveguide resonator is $\nu_r = 6.445$ GHz. For the experiment, the qubit was tuned to a transition frequency of $\omega_a/2\pi = 4.549$ GHz, well into the dispersive limit. At sufficient drive amplitude, time resolved Rabi oscillations are observed on the blue sideband transition by applying microwave square pulses of fixed amplitude and varying the length. The qubit excited state population is then measured by applying a microwave pulse to the resonator after the Rabi-pulse. A π-pulse onto the qubit at the end allows to normalize the population. Figure 4.5 shows the extracted excited state population for the transition, average of 6.6×10^4 repetitions. The blue data points show the results obtained when the system is initially in its ground state $|g, 0\rangle$, the solid line shows the master equation simulation of the time evolution, using values for the qubit relaxation rate $\gamma/2\pi = 0.24$ MHz and photon decay rate $\kappa/2\pi = 1.95$ MHz. The frequency of the Rabi oscillation is given by 6.95 MHz as a fit parameter. At long times the qubit excited state population tends to a steady state value, which can be explained by looking at the two different decay channels in the system as shown in the inset. Since the photon decay rate is much larger than the qubit relaxation rate ($\kappa >> \gamma$), the decay channel with the transition $|e, 1\rangle \rightarrow |e, 0\rangle$ is favored which therefore results in a build up population of the population in the state $|e, 0\rangle$.

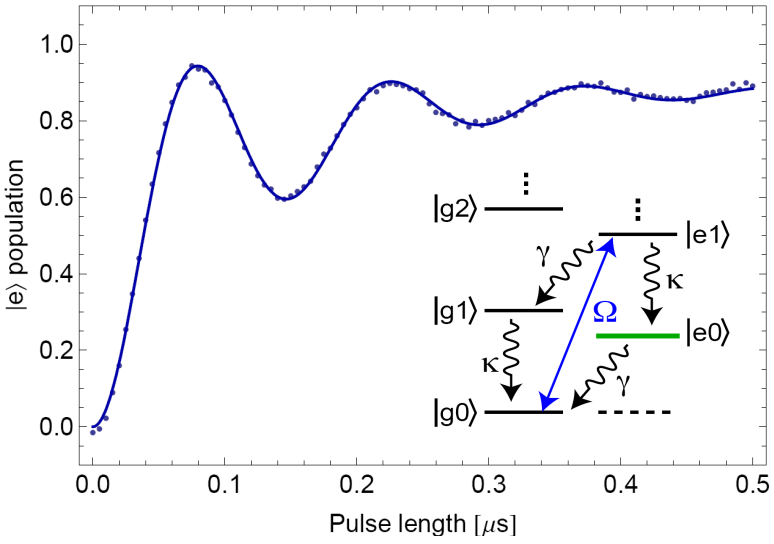

Figure 4.5: Blue sideband transition, done with square pulses of length between 0 ns and 200 ns. Qubit was tuned to a transition frequency of 4.549 GHz. Blue points correspond to the time resolved measurement of the excited state population of the qubit as a function of the pulse length. Solid blue line shows the master equation simulations. Inset: Level diagram showing competing drive and decay rates in the system.

To show full control of the phase of the qubit, we changed the phase of the pulse by

$\pi/2$ after 35 ns. Notice that 2 photons are involved in the sideband transitions such that the total phase shift is π. As one can see in Figure 4.6, there is a good agreement with the theoretical prediction. The blue points and solid line is again the response of a Rabi pulse with different length and the red points and solid line correspond to a total phase shift of π after 35 ns.

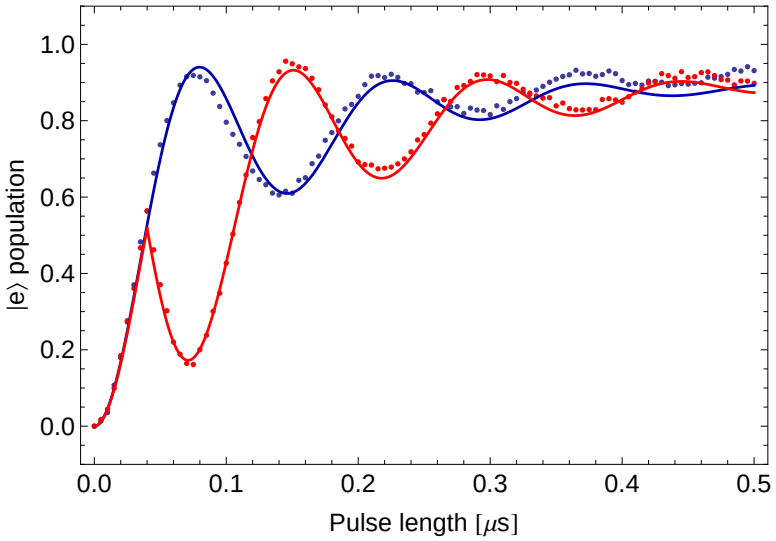

Figure 4.6: Blue sideband transition, done with square pulses of length between 0 ns and 500 ns. Qubit was tuned to a transition frequency of 4.549 GHz. Blue points correspond to the measurement of the sideband Rabi pulses. Red points: By changing the total phase around π after 35 ns, the response function is mirrored. Solid lines shows the theoretical prediction.

In a second experiment, we applied two $\pi/2$-pulses with a certain delay time (5 ns and 20 ns), where the phase of the second pulse is swept from 0 to 2π relative to the first pulse. Each pulse has a length of 35 ns. During the pulses, the frequency of the qubit is shifted due to the Stark effect, such that in the rotating frame of the bare qubit frequency (during the delay time) the corresponding vector in the Bloch sphere starts rotating with the difference frequency, the angle of the rotation depends linearly on the delay time between the pulses. The second $\pi/2$-pulse acts then on a rotated vector such that the projection on the z-axis is different. The red curve in Figure 4.7 shows a linear fit to the data points. Notice that 2 photons are involved in the transition, such that one can see 2 full oscillations in figure 4.7 when the phase of one photon is changed between 0 and 360 degrees.

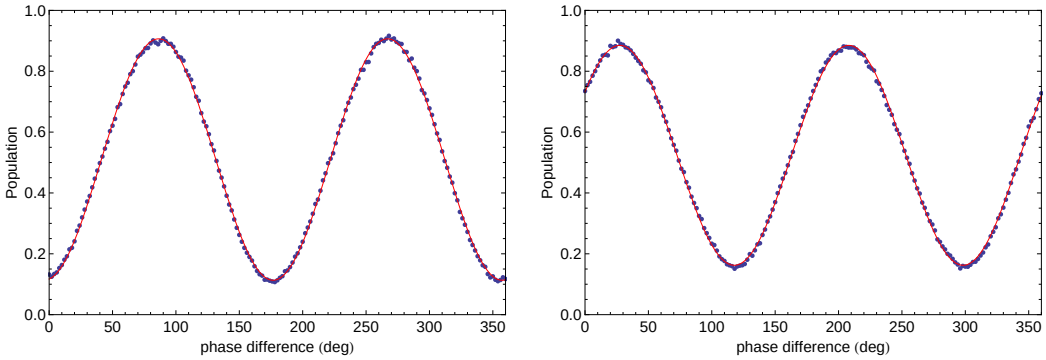

Figure 4.7: Left: Excited state population by applying 2 $\pi/2$-pulses with a delay time of 5 ns, where the phase of the second pulse is swept relative to the first one. Each pulse has a length of 35 ns. Right: Delay time between the two pulses is 20 ns. Red curve is a sinusoidal fit.

5 Conclusion

The main goal of this thesis was the generation of amplitude and phase controlled microwave pulses for qubit manipulation, which could be reached by calibrating an IQ-mixer. The full phase and amplitude control was demonstrated in different experiments. Furthermore, a new setup for sideband-operations was installed and tested by demonstrating the blue-sideband transition $|g,0\rangle \rightarrow |g,1\rangle$.

The task of the IQ-mixer in this work was to upconvert the envelope of a pulse, generated in an arbitrary waveform generator with a low carrier frequency, to a pulse with a high carrier frequency. But the mixing process itself generates unwanted nonlinearities (so-called intermodulation distortions) which is due to the non-linear current-voltage-dependence of a Schottky-diode, the fundamental circuit element of every mixer. Beside this nonlinearites, one also get a signal at the output port which has the frequency corresponding to the LO input signal, but by applying two DC voltages on the two IF-ports one can minimize this disturbing signal. Another signal results from the imbalances of the amplitudes and relative phase of the IF-signals which is then visible as an additional signal with a frequency of $f_{LO} + f_{IF}$, but also this signal can be minimized by an accurate phase and amplitude calibration of the mixer. A Labview program has been written to automate this amplitude and phase calibration for different amplitudes on each IF-channel. The phase- and amplitude imbalances were measured. A fixed relative phase and a constant amplitude correction term can take into account the imbalances for different amplitudes on the I and Q port, but only if the IF- and the LO-frequencies are unchanged. The best result of the calibration can be achieved if the peak-to-peak voltages of the IF-ports are below 600 mV to avoid the nonlinear regime of the IQ-mixer.

The two dimensional one-qubit-tomography was used to show that the phase and amplitude of the square-pulses could be changed independently with four different initial qubit states. Also the new setup with additional high-gain amplifiers could demonstrate a phase-sensitive measurements onto the blue-sideband transition which are all in good agreement with the theoretical prediction.

6 Acknowledgement

First I would like to thank Prof. Andreas Wallraff who gave me the opportunity to write my master thesis in his research group. He always had time to answer my questions and gave me a lot of inspiring advices and improvement suggestions. I also want to thank him for the detailed correction of my written part. But I also got a big support of my collaborators in the group. Especially Dr. Peter Leek, who had to answer a lot of questions, gave me great crash courses at the beginning of my work and introduced me into "Cleansweep" (this is the software used to control the experiment). Matthias Baur spent a lot of time with me in the Laboratory to do the measurements on the qubit and was a great help to write the calibration software in Labview, he also did some of phase sensitive measurements of the sideband transition. Lars Steffen showed me a lot of Mathematica tricks and helped me to extract the informations out of the data files. Romeo Bianchetti taught me about the experimental setup and aided me with analyzing the pulses. Thank you all, it was a pleasure working with you in such a fascinating topic of the current research.

Bibliography

[1] B.D.Josephson. The discovery of tunnelling supercurrentss. *Rev. Mod. Phys.*, pages 251–254, 1974.

[2] Bladh, Duty, Gunnarsson, and Delsing. The single cooper-pair box as a charge qubit. *New Journal of Physics*, 7:180, 2005.

[3] A. Blais, R.-S. Huang, A. Wallraff, S. M. Girvin, and R. J. Schoelkopf. Cavity quantum electrodynamics for superconducting electrical circuits: An architecture for quantum computation. *Physical Review A*, 69(6):062320, June 2004.

[4] J. Carr and G. Carr. *RF components and circuits*. Newnes, April 2002.

[5] John Clarke and Frank K. Wilhelm. Superconducting quantum bits. *Nature*, 453(7198):1031–1042, June 2008.

[6] Johannes Fink. Single qubit control and observation of Berry's phase in a superconducting quantum circuit. Master's thesis, Universität Wien, 2007.

[7] A. Fragner. Coupling superconducting qubits to tunable cavities and resolving the lamb shift in circuit qed. Master's thesis, ETH Zuerich Technische Universitaet Wien, 2008.

[8] A. Fragner, M. Goppl, J. M. Fink, M. Baur, R. Bianchetti, P. J. Leek, A. Blais, and A. Wallraff. Resolving Vacuum Fluctuations in an Electrical Circuit by Measuring the Lamb Shift. *Science*, 322(5906):1357–1360, 2008.

[9] Hermann Haken and Hans Christoph Wolf. *Atom- und Quantenphysik: Einfuehrung in die experimentellen und theoretischen Grundlagen*. Springer, Berlin, 8 edition, 2004.

[10] Ibach and Lueth. *Festkoerperphysik*. Springer, 2002.

[11] Jens Koch, Terri M. Yu, Jay Gambetta, A. A. Houck, D. I. Schuster, J. Majer, Alexandre Blais, M. H. Devoret, S. M. Girvin, and R. J. Schoelkopf. Charge-insensitive qubit design derived from the Cooper pair box. *Physical Review A*, 76(4):042319, 2007.

[12] P. J. Leek, S. Filipp, Maurer P., and A. Wallraff. Entangled state generation in circuit qed using sideband transitions. in preparation, 2008.

[13] A. Lupascu, S. Saito, T. Picot, P. C. de Groot, C. J. P. M. Harmans, and J. E. Mooij. Quantum non-demolition measurement of a superconducting two-level system. *Nat Phys*, 3(2):119–125, February 2007.

[14] Peter Maurer. State tomography of multiple qubits in circuit qed. Master's thesis, ETH Zuerich, 2008.

[15] Mini-Circuits. Modern definition of terms, 08 1999.

[16] Mini-Circuits. Understanding mixers, terms defined, and measuring performance, 2008.

[17] Michael A. Nielsen and Isaac L. Chuang. *Quantum Computation and Quantum Information*. Cambridge Univertity Press, 2000.

[18] D. M. Pozar. *Microwave Engineering*. Addison-Wesley Publishing Company, 1993.

[19] D. I. Schuster. *Circuit Quantum Electrodynamics*. PhD thesis, Yale University, 2007.

[20] F. Schwabl. *Quantenmechanik*. Springer, 2002.

[21] R. N. Simons. *Coplanar waveguide circuits, components and systems*. Wiley Series in Microwave and Optical Engineerging. Wiley Inter-Science, 2001.

[22] S.Shapiro. Josephson currents in superconducting tunneling: The effect of microwaves and other observations. *Phys. Rev.Lett.*, 11:80–82, 1963.

[23] Lars Steffen. Local qubit control in circuit quantum electrodynamics. Master's thesis, ETH Zuerich, 2008.

[24] M. Tinkham. *Introduction to Superconductivity*. McGraw-Hill International Editions, 1996.

[25] A. Wallraff, D. I. Schuster, A. Blais, J. M. Gambetta, J. Schreier, L. Frunzio, M. H. Devoret, S. M. Girvin, and R. J. Schoelkopf. Sideband transitions and two-tone spectroscopy of a superconducting qubit strongly coupled to an on-chip cavity. *Physical Review Letters*, 99:050501, 2007.

[26] Andreas Wallraff, Hannes Majer, Luigi Frunzio, and Robert Schoelkopf. Superconducting solid state cavity QED: Notes on resonators. 2003.

[27] D.F. Walls and G.J. Milburn. *Quantum optics*. Spinger-Verlag, Berlin, 1994.

[28] K. Yoshida, K. Watanabe, T. Kisu, and K. Enpuku. Evaluation of magnetic penetration depth and surface resistance of superconducting thin films using coplanar waveguides. *IEEE Trans. Appl. Supercond.*, 5(2):1979–1982, 1995.